The Astrophysical Journal, 976:178 (21pp), 2024 December 1 https://doi.org/10.3847/1538-4357/ad8448

The Extremely Metal-poor SN 2023ufx: A Local Analog to High-redshift Type II Supernovae

Michael A. Tucker[1,2,15], Jason Hinkle[3,16], Charlotte R. Angus[4], Katie Auchettl[5,6], Willem B. Hoogendam[3,17], Benjamin Shappee[3], Christopher S. Kochanek[1,2], Chris Ashall[3,7], Thomas de Boer[3], Kenneth C. Chambers[3], Dhvanil D. Desai[3], Aaron Do[8], Michael D. Fulton[4], Hua Gao[3], Joanna Herman[3], Mark Huber[3], Chris Lidman[9], Chien-Cheng Lin[3], Thomas B. Lowe[3], Eugene A. Magnier[3], Bailey Martin[9], Paloma Mínguez[3], Matt Nicholl[4], Miika Pursiainen[10], S. J. Smartt[4,11], Ken W. Smith[4], Shubham Srivastav[11], Brad E. Tucker[12,13,14], and Richard J. Wainscoat[3]

[1] Center for Cosmology and AstroParticle Physics, 191 W Woodruff Avenue, Columbus, OH 43210, USA; tuckerma95@gmail.com
[2] Department of Astronomy, The Ohio State University, 140 W 18th Avenue, Columbus, OH 43210, USA
[3] Institute for Astronomy, University of Hawai'i, 2680 Woodlawn Drive, Honolulu, HI 96822, USA
[4] Astrophysics Research Centre, School of Mathematics and Physics, Queen's University Belfast, Belfast BT7 1NN, UK
[5] School of Physics, The University of Melbourne, VIC 3010, Australia
[6] Department of Astronomy and Astrophysics, University of California, Santa Cruz, CA 95064, USA
[7] Department of Physics, Virginia Tech, 850 West Campus Drive, Blacksburg, VA 24061, USA
[8] Institute of Astronomy and Kavli Institute for Cosmology, Madingley Road, Cambridge, CB3 0HA, UK
[9] The Research School of Astronomy and Astrophysics, The Australian National University, ACT 2601, Australia
[10] Department of Physics, University of Warwick, Gibbet Hill Road, Coventry CV4 7AL, UK
[11] Astrophysics sub-Department, Department of Physics, University of Oxford, Keble Road, Oxford OX1 3RH, UK
[12] Mt Stromlo Observatory, The Research School of Astronomy and Astrophysics, Australian National University, ACT 2611, Australia
[13] National Centre for the Public Awareness of Science, Australian National University, ACT 2601, Australia
[14] The ARC Centre of Excellence for All-Sky Astrophysics in 3 Dimension (ASTRO 3D), Australia
Received 2024 April 30; revised 2024 September 16; accepted 2024 September 23; published 2024 November 21

Abstract

We present extensive observations of the Type II supernova (SN II) SN 2023ufx, which is likely the most metal-poor SN II observed to date. It exploded in the outskirts of a low-metallicity ($Z_{\rm host} \sim 0.1\ Z_{\odot}$) dwarf ($M_g = -13.39 \pm 0.16$ mag, $r_{\rm proj} \sim 1$ kpc) galaxy. The explosion is luminous, peaking at $M_g \approx -18.5$ mag, and shows rapid evolution. The *r*-band (pseudobolometric) light curve has a shock-cooling phase lasting 20 (17) days followed by a 19 (23) day plateau. The entire optically thick phase lasts only ≈55 days following explosion, indicating that the red supergiant progenitor had a thinned H envelope prior to explosion. The early spectra obtained during the shock-cooling phase show no evidence for narrow emission features and limit the preexplosion mass-loss rate to $\dot{M} \lesssim 10^{-3}\ M_{\odot}\ {\rm yr}^{-1}$. The photospheric-phase spectra are devoid of prominent metal absorption features, indicating a progenitor metallicity of $\lesssim$0.1 $Z_{\odot}$. The seminebular (∼60–130 days) spectra reveal weak Fe II, but other metal species typically observed at these phases (Ti II, Sc II, and Ba II) are conspicuously absent. The late-phase optical and near-infrared spectra also reveal broad (≈10^4 km s^{-1}) double-peaked Hα, Pβ, and Pγ emission profiles suggestive of a fast outflow launched during the explosion. Outflows are typically attributed to rapidly rotating progenitors, which also prefer metal-poor environments. This is only the second SN II with $\lesssim$0.1 $Z_{\odot}$ and both exhibit peculiar evolution, suggesting a sizable fraction of metal-poor SNe II have distinct properties compared to nearby metal-enriched SNe II. These observations lay the groundwork for modeling the metal-poor SNe II expected in the early Universe.

Unified Astronomy Thesaurus concepts: Nucleosynthesis (1131); Metallicity (1031); Interacting binary stars (801); Type II supernovae (1731); Stellar jets (1607); Stellar winds (1636)

Materials only available in the online version of record: data behind figures

1. Introduction

H-rich Type II supernovae (SNe II) originate from the core collapse (CC) of red supergiants (RSGs; S. J. Smartt 2009; S. J. Smartt et al. 2009). Observations within the first ∼week probe the cooling of the shock-heated envelope (the shock-cooling phase; e.g., N. Sapir & E. Waxman 2017) before the ejecta transitions to the plateau phase where recombination of H in the shock-ionized envelope produces a quasi-constant optical luminosity (S. W. Falk & W. D. Arnett 1977). Plateau-phase spectra are characterized by prominent P Cygni Balmer features and absorption from various metal species such as Fe, Sc, and Ba (e.g., C. P. Gutiérrez et al. 2017a). The light curve transitions to a radioactive-decay tail after the recombination wave reaches the He zone where the observed emission is powered by the radioactive decay of ^{56}Co. Nebular spectra constrain the mass of the progenitor star through the strength of emission lines from intermediate-mass elements (i.e., O and Ca; e.g., A. Jerkstrand et al. 2012, 2014). Calibrated to progenitor stars identified in preexplosion imaging

[15] CCAPP Fellow.
[16] NASA FINESST Future Investigator.
[17] NSF Graduate Research Fellow.

(e.g., W. Li et al. 2005; S. Mattila et al. 2008; J. R. Maund et al. 2014; C. S. Kochanek et al. 2017; C. D. Kilpatrick & R. J. Foley 2018), there is growing agreement between SN II models and observations (e.g., L. Dessart et al. 2013, 2017; V. P. Utrobin et al. 2017; L. Martinez & M. C. Bersten 2019).

The duration of the plateau phase ($\Delta t_{\rm pl}$) primarily depends on the mass of the H envelope ($M_{\rm env}$) with minor contributions from the explosion energy and synthesized ^{56}Ni mass ($M_{\rm Ni}$; D. V. Popov 1993; D. Kasen & S. E. Woosley 2009). SNe II are observationally classified according to their plateau durations. On the long end of the $\Delta t_{\rm pl}$ distribution are the canonical Type IIP SNe (SNe IIP) exhibiting $\Delta t_{\rm pl} \sim 80$–120 days (e.g., B. L. Barker et al. 2022). Type IIb SNe (SNe IIb), with negligible H envelopes, occupy the short end of the $\Delta t_{\rm pl}$ distribution ($\Delta t_{\rm pl} \sim 0$ days; R. A. Chevalier & A. M. Soderberg 2010; A. Gilkis & I. Arcavi 2022) and the intermediate short-plateau and Type IIL SNe (SNe IIL) have thin H envelopes (e.g., D. Hiramatsu et al. 2021). Theoretically, decreasing plateau durations correspond to lower $M_{\rm env}$. SNe II with $\Delta t_{\rm pl} \lesssim 80$ days suggest the RSG had a thinner H envelope than expected from a typical 10–20 $M_\odot$ SN II progenitor. This can be interpreted as a mass sequence of SN II progenitors where more massive stars have stronger stellar winds that more efficiently remove their envelopes (e.g., C. de Jager et al. 1988; J. S. Vink et al. 2001; J. S. Vink 2022) or due to interaction with a nearby binary companion (e.g., J. J. Eldridge et al. 2018; L. Dessart et al. 2024). Disentangling these effects remains a major difficulty in understanding massive-star formation and (co-)evolution (e.g., N. Langer 2012; N. Smith 2014).

Progenitor metallicity (Z) is another poorly constrained aspect of massive-star evolution (e.g., D. Sanyal et al. 2017; S.-H. Chun et al. 2018; G. Volpato et al. 2023) and their SNe (L. Dessart et al. 2013, 2014; D. Ibeling & A. Heger 2013). For a given zero-age main-sequence mass, reduced metallicity lowers the mass-loss rate with $\dot{M} \propto Z^{\alpha}$ and $\alpha \sim 0.3$–0.8 (e.g., J. S. Vink et al. 2001; M. R. Mokiem et al. 2007; A. A. C. Sander et al. 2020; J. S. Vink 2022) leading to more massive and compact progenitors (T. Sukhbold & S. E. Woosley 2014; M. Limongi & A. Chieffi 2018; A. Aryan et al. 2023). This has implications for stellar feedback (e.g., M. C. Jecmen & M. S. Oey 2023; P.-S. Ou et al. 2023), ionizing photon production (e.g., Y. Götberg et al. 2017), and nucleosynthesis (e.g., A. Heger & S. E. Woosley 2010; M. Limongi & A. Chieffi 2018). The influence of Z on massive-star evolution is supported by observed correlations between host-galaxy/environmental metallicity and SN II spectral features (J. L. Prieto et al. 2008; L. Dessart et al. 2014; J. P. Anderson et al. 2016; L. Galbany et al. 2016; F. Taddia et al. 2016; T. Pessi et al. 2023). Low-metallicity and/or dwarf-galaxy SNe II are typically more luminous than the broader population (e.g., I. Arcavi et al. 2010; C. P. Gutiérrez et al. 2018; S. Scott et al. 2019). Yet these observed correlations are mostly confined to ensemble analyses of heterogeneous observations that are skewed toward higher-metallicity environments. This is simply a reflection of bright SNe exploding in luminous nearby galaxies where the average stellar population has near-solar composition. This observational bias also likely accounts for the dearth of $Z \lesssim 0.3\ Z_\odot$ SNe II in the samples of L. Dessart et al. (2014) and J. P. Anderson et al. (2016), who relied on observational campaigns targeting nearby galaxies. Even the untargeted iPTF sample of F. Taddia et al. (2016) only contained a handful (∼5 out of 39) of candidate low-metallicity SNe II. SN 2015bs (J. P. Anderson et al. 2018) is the only known SN II with a reliable metallicity $\lesssim 0.1\ Z_\odot$ but lacks extensive spectroscopic observations. As we push deeper into the early Universe with JWST (e.g., K. Boyett et al. 2022; M. W. Topping et al. 2022), a holistic understanding of metal-poor massive stars, their SNe, and subsequent feedback is paramount.

Table 1
Basic Properties of SN 2023ufx and Its Host

Parameter	Value
SN 2023ufx	
R.A. [hms]	08:24:51.6
Decl. [dms]	+21:17:43.2
R.A. [deg]	126.2148658
Decl. [deg]	+21.2953198
Explosion date [MJD]	60223.0 ± 0.5
Peak m_g [mag]	15.55 ± 0.02
Peak M_g [mag]	-18.54 ± 0.15
$E(B-V)_{\rm MW}$ [mag]	0.04
$E(B-V)_{\rm host}$ [mag]	0[a]
Host Galaxy	
Redshift z	0.0152 ± 0.0001
Distance [Mpc]	65.9 ± 4.4
Distance modulus [mag]	34.09 ± 0.15
M_g [mag]	-13.39 ± 0.16
M_r [mag]	-13.47 ± 0.17
Observed r-band radius [arcsec]	3.1 ± 0.3
Intrinsic r-band radius [kpc]	1.0 ± 0.1
$\log_{10}$([O III] λ5007/Hβ) [dex]	0.02 ± 0.06
$\log_{10}$([O II] λ3727/Hβ) [dex]	0.45 ± 0.06
$\log_{10}$([N II] λ6584/Hα) [dex]	$<-1.8(3\sigma)$
$\log_{10}$([O I] λ6300/Hα) [dex]	$<-2.0(3\sigma)$
$\log_{10}$([S II] λ6717, 6734/Hα) [dex]	-1.05 ± 0.09
$\log_{10}$(O/H) + 12 [dex]	$\lesssim 8$
Host A_V [mag]	$0.00^{+0.09}_{-0.00}$
$\log_{10}$(Age [yr])	$8.0^{+0.4}_{-0.2}$
$\log_{10}$(Mass [$M_\odot$])	$6.4^{+0.1}_{-0.1}$
$\log_{10}$(SFR [$M_\odot$ yr^{-1}])	$-6.6^{+4.1}_{-2.8}$

Note.
[a] Adopted (see Section 3).

Here we present follow-up observations and analysis of the luminous, fast-evolving, and metal-poor SN II SN 2023ufx. The observations and data reductions procedures are summarized in Section 2. We analyze the host-galaxy properties in Section 3, finding that SN 2023ufx exploded in the outskirts of a metal-poor dwarf galaxy. We analyze the photometric and spectroscopic observations of SN 2023ufx in Section 4 and Section 5, respectively. We place SN 2023ufx in broader context and discuss its implications in Section 6. We review our findings in Section 7. A full accounting of the data and calibration are given in Appendix A. Additional figures and tables are included in Appendix B along with the references for the comparison SNe. The main properties of SN 2023ufx and its host are summarized in Table 1.

2. Observations

SN 2023ufx was discovered by the Asteroid Terrestrial-impact Last Alert System (ATLAS; J. L. Tonry et al. 2018b;

K. W. Smith et al. 2020) on UT 2023 October 6 13:55:52 (MJD 60223.58) at $o \approx 18.8$ mag (internal designation ATLAS23tsa). We summarize the photometry and spectroscopy here and provide a detailed accounting of the data reduction and calibration in Appendix A. All observations are corrected for Milky Way reddening of $E(B-V) = 0.04$ (E. F. Schlafly & D. P. Finkbeiner 2011) using $R_V = 3.1$ and the wavelength dependence of E. L. Fitzpatrick (1999). No correction for host-galaxy extinction is applied because it is negligible based on the consistency of the early spectra with an unreddened blackbody, the lack of Na I absorption at the host redshift, and the distance of SN 2023ufx from the host.

We collect survey light curves including *c*- and *o*-band photometry from ATLAS, *g*-band photometry from the All-Sky Automated Survey for SuperNovae (ASAS-SN; B. J. Shappee et al. 2014), *g*- and *r*-band photometry from the Zwicky Transient Facility (ZTF; E. C. Bellm et al. 2019), and *grizyw* photometry from the Panoramic Survey Telescope and Rapid Response System (Pan-STARRS; K. C. Chambers et al. 2016). Daily average fluxes are computed for surveys with more than one observation per night but we do not combine across different surveys (e.g., ZTF *g* and Pan-STARRS *g*) due to small differences in system throughputs. Additional photometric observations were obtained with the Neil Gehrels Swift Observatory (Swift) UltraViolet and Optical Telescope (UVOT; N. Gehrels et al. 2004; P. W. A. Roming et al. 2005) and the Multi-Object Double Spectrograph (MODS; R. W. Pogge et al. 2010). The Swift observations cover the *UVW*2, *UVM*2, *UVW*1, *U*, *B*, and *V* filters and the MODS imaging used the *ugri* filters.

Multiple epochs of optical and near-infrared (NIR) spectra were obtained for SN 2023ufx. The earliest spectrum was obtained ≈2.5 days after discovery, or ≈3.5 days relative to the estimated explosion epoch, by the Spectroscopic Classification of Astronomical Transients (SCAT; M. A. Tucker et al. 2022) survey using the SuperNova Integral Field Spectrograph (SNIFS; B. Lantz et al. 2004) on the University of Hawai'i 2.2 m (UH2.2m) telescope. Other sources of optical spectra include the MODS (R. W. Pogge et al. 2010) on the Large Binocular Telescope (LBT), the Keck Cosmic Web Imager (KCWI; P. Morrissey et al. 2018) on the Keck II telescope, the Wide-Field Spectrograph (WiFeS; M. Dopita et al. 2007, 2010) on the Australian National University 2.3 m (ANU2.3m) telescope, the Gemini Multi-Object Spectrograph (GMOS; I. M. Hook et al. 2004) on the Gemini-North (GN) telescope, and the Alhambra Faint Object Spectrograph (ALFOSC)[18] on the Nordic Optical Telescope (NOT). Three epochs of NIR spectra were obtained with SpeX (J. T. Rayner et al. 2003) on NASA's Infrared Telescope Facility (IRTF). The full spectroscopic time series extends until ≈130 days after explosion. Host-galaxy spectra were extracted from the later KCWI 3D (x, y, λ) data cubes once SN 2023ufx had faded sufficiently. Complete details about the data reduction and calibration are provided in Appendix A.

3. Host-galaxy Properties

Figure 1 shows the host galaxy of SN 2023ufx. SDSS J082451.43+211743.3 is a faint ($g = 20.86 \pm 0.04$ mag) extended blue source with an absolute *g*-band luminosity of $M_g = -13.23 \pm 0.16$ mag. The galaxy is small, with a *g*-band Kron radius (R. G. Kron 1980) of just $R_g = 3\farcs6$ corresponding to a projected intrinsic radius of 1.1 kpc. SN 2023ufx exploded ≈$2\farcs7$ (∼0.8 kpc) from the nucleus. The host-galaxy parameters are summarized in Table 1.

SN 2023ufx was originally considered a potential fast blue optical transient (see AstroNotes 268, 269, and 278) based upon the SDSS photometric redshift of $z_{\rm phot} \approx 0.04$. Instead, the true redshift is $z \approx 0.015$ (AstroNote 292). Fitting the [O II] λ3727, [O III] $\lambda\lambda$4959, 5007, Hβ, Hα, and [S II] $\lambda\lambda$6716, 6731 host-galaxy emission lines in the late-time KCWI observations produces a refined redshift of $z = 0.0152 \pm 0.0001$. At this redshift, the host galaxy is located at $d \approx 65.9 \pm 4.4$ Mpc based on the dynamical velocity-field estimate of E. J. Shaya et al. (2022), corresponding to a distance modulus of 34.09 ± 0.15 mag using cosmological parameters $H_0 = 70$ km s^{-1} Mpc^{-1} and $\Omega_{\rm M} = 0.3$.

The host-galaxy spectrum is dominated by these strong emission lines. The continuum is marginally detected in the blue channel of the last KCWI observations ($\lesssim$5000 Å) but only emission lines are detected in the red channel. This is expected given the $\gtrsim$20 to 1 SN-to-galaxy flux ratio at redder wavelengths in the latest KCWI observation. Importantly, [N II] λ6584 is only marginally ($\sim 3\sigma$) detected.

The [O III] λ4363 feature is not detected so we must rely on empirical strong-line metallicity estimates. We adopt $\log_{10}({\rm O/H}) + 12 \lesssim 8$ dex based on $\log_{10}([{\rm N\,II}]/{\rm H}\alpha) < -1.8$ dex. This corresponds to $\log_{10}(Z_{\rm host}/Z_\odot) \lesssim -0.9$ dex using the solar abundances from M. Asplund et al. (2021). The low host-galaxy metallicity is supported by where it lies in the relations between metallicity and galaxy luminosity (e.g., I. Arcavi et al. 2010; N. E. Sanders et al. 2013). The faintness of the host ($M_{g,r} \approx -13$ mag) places it outside the bounds of the calibration samples for these relations, but extrapolating to such faint dwarfs (as done by J. P. Anderson et al. 2018 for the host of the metal-poor SN II SN 2015bs) produces a similar global metallicity estimate of $\log_{10}(Z_{\rm host}/Z_\odot) = -1.3 \pm 0.3$ dex.

We derive integrated host-galaxy properties by fitting the host-galaxy photometry from the Galaxy Evolution Explorer (D. C. Martin et al. 2005; P. Morrissey et al. 2007), Sloan Digital Sky Survey (SDSS; D. G. York 2000), and the Wide-field Infrared Survey Explorer (E. L. Wright et al. 2010) using FAST (M. Kriek et al. 2009) with free parameters for the total stellar mass, stellar age, internal extinction, star formation rate (SFR), and the star formation history modeled as a delayed exponential. Parameters with meaningful constraints are included in Table 1. The low mass of the galaxy will be discussed further in Section 6.1.

4. Photometric Properties

4.1. Preexplosion and Discovery

SN 2023ufx was discovered by ATLAS on MJD 60223.58. The public ZTF data stream reports a stringent nondetection ≈1 day prior so we adopt the midpoint of these two observations, MJD 60223.0 ± 0.5, as the estimated explosion epoch, where the uncertainty spans the full range of possible explosion times. SN 2023ufx did not experience any detectable outbursts in the ≈8 yr prior to explosion. Assuming an outburst would produce enhanced flux for more than a single night, we also compute 30 day averages of the single-epoch fluxes to better constrain fainter events. The 30 day window is motivated by objects with observed preexplosion variability (e.g., W. V. Jacobson-Galán et al. 2022; D. Hiramatsu et al. 2023) but modifying the length of

[18] https://www.not.iac.es/instruments/alfosc/

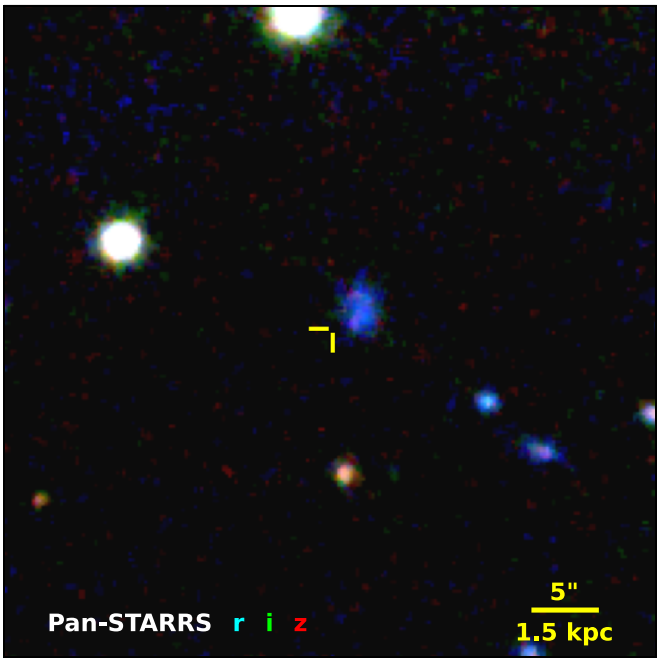

Figure 1. Preexplosion imaging of the host galaxy from Pan-STARRS. Yellow reticles are 1″ (0.3 kpc) in length and mark the location of SN 2023ufx.

the averaging window does not affect our conclusions. The median limits on the preexplosion luminosity are given in Table 2.

The time required for the light curve to reach peak brightness is correlated with the progenitor radius (e.g., I. Rabinak & E. Waxman 2011; V. Morozova et al. 2016). The rising light curve is poorly sampled with only a single ATLAS *o*-band measurement but we synthesize *g*- and *o*-band fluxes from the first SNIFS observations ≈2.5 days after discovery (≈3.5 days after explosion). We measure a *g*-band rise time of 5 ± 1 days, which is only slightly shorter than typical SNe II (e.g., S. Gonzalez-Gaitan et al. 2015). Using the relation between *g*-band rise time and progenitor radius derived by V. Morozova et al. (2016) we find a preexplosion radius of $R_\star \approx 350\ R_\odot$, albeit with large uncertainties and the caveat that the relation was calibrated to SNe IIP and may not accurately describe fast-evolving SNe II.

4.2. Rapid Evolution

SN 2023ufx peaked at $B/g \approx 15.5$ mag corresponding to $M_{g/B} \approx -18.5$ mag (Figure 2), more luminous than most SNe II (e.g., J. P. Anderson et al. 2014; S. Valenti et al. 2016), but consistent with metal-poor dwarf galaxies hosting overluminous SNe II (e.g., C. P. Gutiérrez et al. 2018; S. Scott et al. 2019). The most notable aspect of the light curve is the short plateau duration seen in Figure 2 spanning ∼10 days and ∼15 days in the *g* and *r* bands, respectively. Figure 3 shows a piecewise fit (e.g., N. E. Sanders et al. 2015) to the *r*-band Pan-STARRS and ZTF observations. The fit divides the evolution into three phases: the shock-cooling phase ($\Delta t_{\rm sc}$), the plateau phase ($\Delta t_{\rm pl}$), and the transition from the plateau to the radioactive tail ($\Delta t_{\rm tr}$). There are four corresponding exponential decay coefficients: $\beta_{\rm sc}$ during the shock-cooling phase, $\beta_{\rm pl}$ during the plateau, $\beta_{\rm tr}$ during the transition, and $\beta_{\rm tail}$ for the radioactive tail. The values are given in Table 3.[19]

[19] The fitted decay coefficients can be converted to the light-curve decay parameters introduced by J. P. Anderson et al. (2014): $s_1 \equiv \Delta m_{\rm sc}$, $s_2 \equiv \Delta m_{\rm pl}$, and $s_3 \equiv \Delta m_{\rm tail}$.

Table 2
Median 3σ Limits on Preexplosion Outbursts and Variability from Survey Photometry

Survey/ Filter	Single Epoch			30 Day Average		
	F_ν (μJy)	App. Mag.	Abs. Mag.	F_ν (μJy)	App. Mag.	Abs. Mag.
ZTF-*g*	38.2	19.9	−12.4	4.7	22.2	−11.8
ZTF-*r*	38.5	19.9	−12.4	4.8	22.2	−11.8
ZTF-*i*	44.8	19.8	−14.2	7.7	21.7	−12.3
ATLAS-*c*	36.0	20.0	−14.0	7.6	21.7	−12.3
ATLAS-*o*	38.5	19.9	−14.1	8.2	21.6	−12.4

Note. The ATLAS and ZTF light curves span ≈8 and ≈5 yr prior to explosion, respectively. The light curve is shown in Appendix B.

We also compute the optical pseudobolometric fluxes using the *grizy* Pan-STARRS photometry assuming the emission can be approximated by a blackbody. The combined optical + NIR spectra in Section 5 confirm this is an acceptable assumption even at ∼100 days after explosion. We exclude *r*-band observations ⩾50 days after explosion to prevent the strong Hα emission from biasing the measured luminosities. The $L_{\rm opt}$ light curve is shown alongside the *r*-band light curve in Figure 3 and the piecewise fit parameters are included in Table 3. The short (≈20 days) plateau duration is not due to the strong Hα emission in the *r* band.

The duration of the plateau primarily depends on H envelope mass (e.g., D. Kasen & S. E. Woosley 2009). Increased explosion energy and decreased $M_{\rm Ni}$ can extend or shorten the plateau by ≲10%. Applying the scaling relations of J. A. Goldberg et al. (2019) and Q. Fang et al. (2024) to the *r*-band plateau of SN 2023ufx, we estimate $M_{\rm env} = 0.5$–$1.5\ M_\odot$. This $M_{\rm env}$ estimate is consistent with the modeling estimates of $M_{\rm env} \sim 1.7\ M_\odot$ by D. Hiramatsu et al. (2021) for their sample of three short-plateau SNe II (SNe 2006Y, 2006ai, and 2016egz). However, L. Martinez et al. (2022a, 2022b, 2022c) infer a much higher $M_{\rm env} \sim 7\ M_\odot$ for SN 2006ai despite measuring a similarly short plateau duration (≈40 days) as D. Hiramatsu et al. (2021). These discrepancies highlight the intrinsic difficulty of inferring physical parameters from observables, especially for these faster-evolving SNe II.

Figure 4 shows that SN 2023ufx initially had a similar color evolution to other SNe II, including short-plateau SNe, SNe IIL, and SNe IIP. The color similarity ends when SN 2023ufx enters its early radioactive-decay/nebular phase and develops a strong Hα emission line, leading to the steadily bluer $r - i$ colors at ≳60 days after explosion. The strong Hα emission makes the $g - r$ color very red, but the "intrinsic" color without Hα is relatively bluer at ≳60 days than most SNe. This is probably due to the early nebular transition revealing a hotter core. The early Swift colors (not shown) are indistinguishable from other SNe II, consistent with shock cooling producing the early light curve. Overall, the lack of color deviations from normal SNe II agrees with the models of L. Dessart et al. (2013), where metallicity effects are balanced by trade-offs between a smaller progenitor size (faster expansion cooling) and decreased metal-line blanketing at ≲5000 Å (bluer colors).

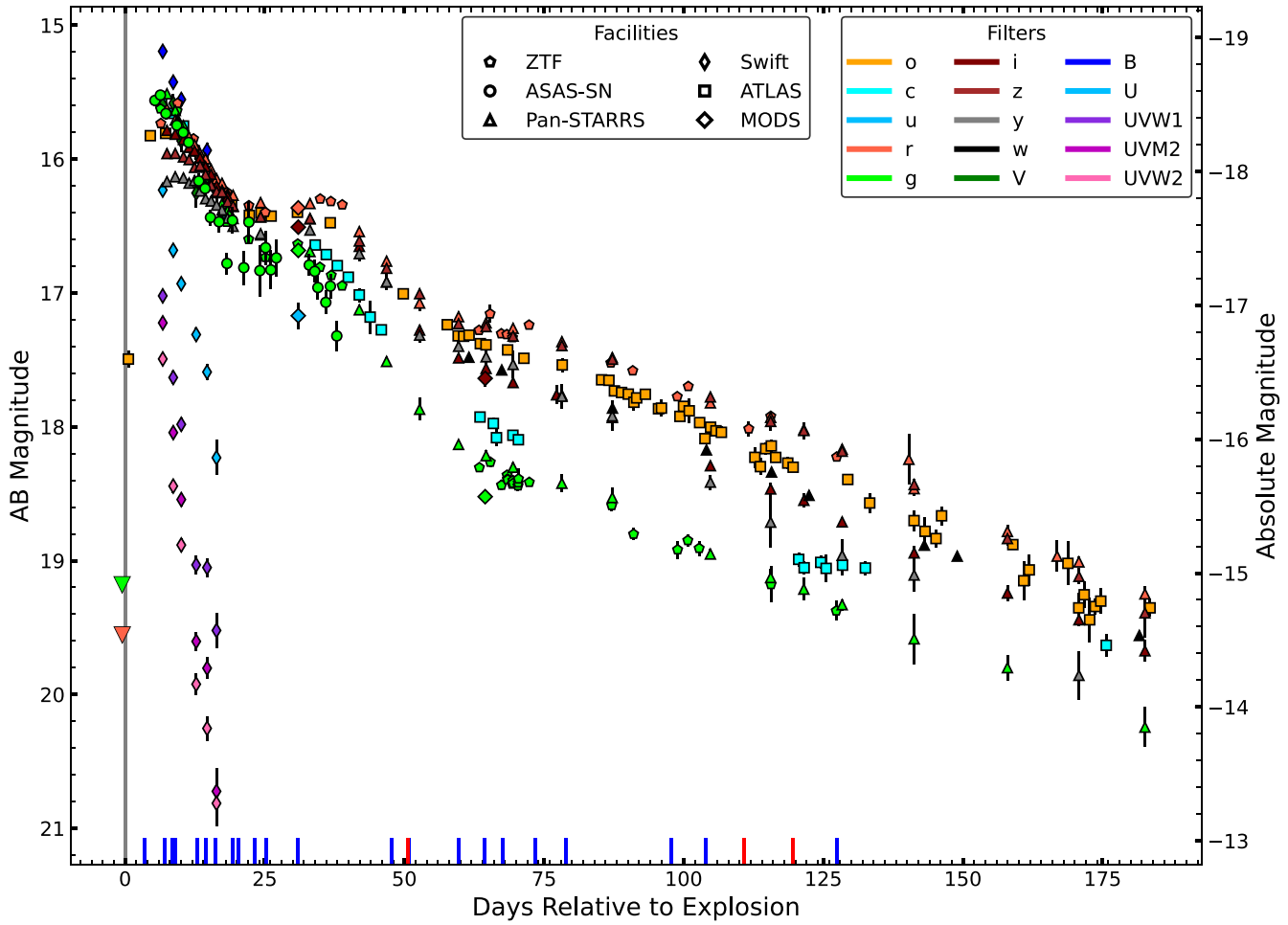

Figure 2. Extinction-corrected light curves of SN 2023ufx. The same colors and symbols are used throughout the manuscript. Inverted triangles show 5σ nondetections ∼0.5 days before explosion from ZTF. Blue and red ticks along the lower axis denote optical and NIR spectroscopic observations, respectively. This light-curve information is available as the data behind the figure.

(The data used to create this figure are available in the online article.)

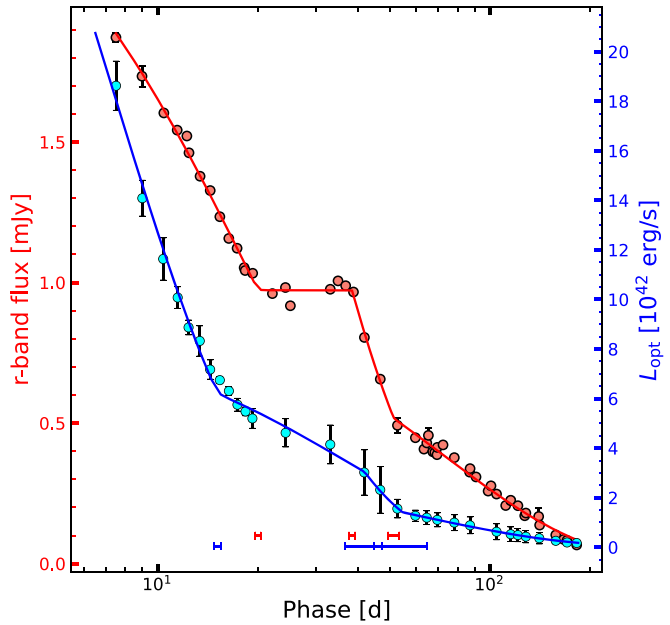

Figure 3. Piecewise fits to the *r*-band fluxes (red, left scale) and the derived L_{opt} (blue, right scale). Colored error bars along the bottom show the estimated transition times between the different phases of light-curve evolution (see Section 4.2).

4.3. ^{56}Ni Mass

The postplateau light-curve evolution traces energy input from the decay of $^{56}\mathrm{Co} \rightarrow {}^{56}\mathrm{Fe}$. We use Equation (2) from M. Hamuy (2003) to estimate the synthesized Ni mass and a Monte Carlo method to incorporate the photometric and distance uncertainties. We find $M_{\mathrm{Ni56}} = 0.13 \pm 0.04\ M_{\odot}$, although the L_{opt} decay ($\Delta m_{tail} \sim 1.4$ mag per 100 days) is steeper than expected for pure ^{56}Co decay powering the observed emission. This ^{56}Ni mass is above average for SNe II but within the plausible range (e.g., M. Hamuy 2003; O. Pejcha & J. L. Prieto 2015; J. P. Anderson 2019) and roughly agrees with the correlation between plateau luminosity and ^{56}Ni mass from T. Müller et al. (2017). The measured M_{Ni} is more consistent with the Type Ib/IIb/Ic SN sample of N. Meza & J. P. Anderson (2020), albeit still above their average values.

5. Spectroscopic Evolution

5.1. Early Spectra

The spectroscopic time series shown in Figure 5 spans ∼3–130 days after explosion. The spectra obtained $\lesssim$15 days after explosion are almost perfect blackbody curves with only minor deviations from weak, broad spectral features, confirming that the early light curve traces the shock-cooling emission

Table 3
Parameters from Fitting a Piecewise Decay to the Optical Fluxes and Blackbody Luminosities (Figure 3)

	Δt_{sc}	Δt_{pl}	Δt_{tr}	$\log_{10}\beta_{sc}$ Δm_{sc}	$\log_{10}\beta_{pl}$ Δm_{pl}	$\log_{10}\beta_{tr}$ Δm_{tr}	$\log_{10}\beta_{tail}$ Δm_{tail}
g band	21.7 ± 1.1	13.8 ± 2.3	22.2 ± 6.0	-1.19 ± 0.02 7.1 ± 0.3	-1.99 ± 0.27 1.1 ± 0.7	-1.23 ± 0.08 6.4 ± 1.2	-1.80 ± 0.11 1.7 ± 0.4
r band	20.1 ± 0.4	18.4 ± 0.7	12.9 ± 1.8	-1.28 ± 0.01 5.7 ± 0.2	-4.4 ± 4.9 0.0 ± 0.1	-1.31 ± 0.05 5.3 ± 0.5	-1.86 ± 0.02 1.5 ± 0.1
o band	21.6 ± 0.8	13.5 ± 1.6	19.4 ± 2.9	-1.46 ± 0.02 3.8 ± 0.2	-9.2 ± 3.3 0.0 ± 0.1	-1.43 ± 0.04 4.1 ± 0.4	-1.82 ± 0.02 1.6 ± 0.1
L_{opt}	15.1 ± 0.4	26.9 ± 5.2	12.7 ± 8.4	-0.85 ± 0.02 15.2 ± 0.5	-1.58 ± 0.08 2.9 ± 0.5	-1.22 ± 0.15 6.6 ± 2.3	-1.80 ± 0.12 1.7 ± 0.5

Note. Durations (Δt_{sc}, Δt_{pl}, and Δt_{tr}) are given in rest-frame days. The second row converts the $\log_{10}\beta$ exponential decay coefficients into the corresponding magnitudes per 100 days (Δm).

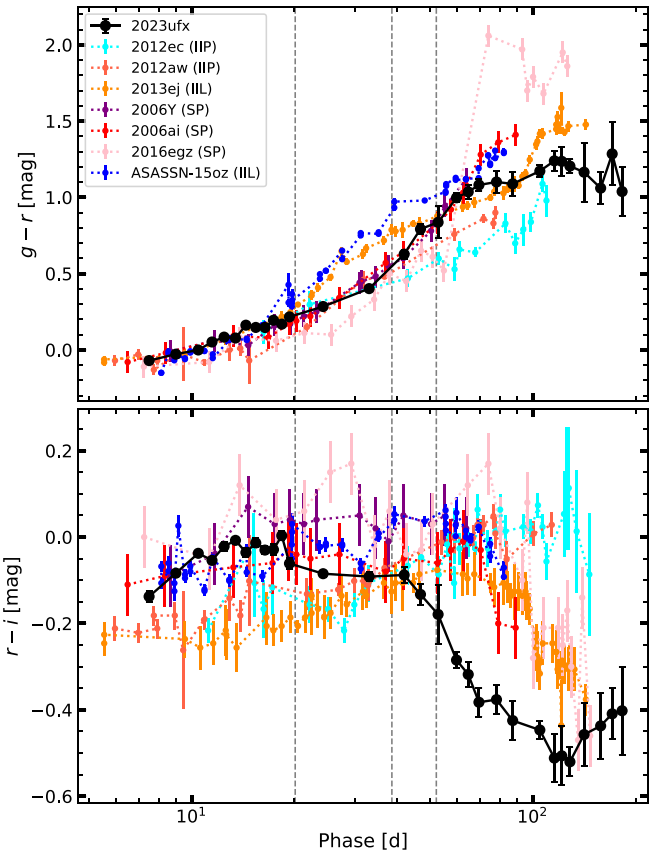

Figure 4. Extinction-corrected color evolution of SN 2023ufx compared to other SNe II. Gray vertical lines mark the different stages of evolution (see Section 4.2).

(e.g., J. Morag et al. 2024). Some SNe II show narrow emission lines in the early ($\lesssim$10 days) spectra (e.g., R. J. Bruch et al. 2023; W. V. Jacobson-Galán et al. 2023) due to the shock breakout radiation pulse photoionizing the circumstellar medium (CSM) near the stellar surface (e.g., D. Khazov et al. 2016; C. S. Kochanek 2019). No such features are seen in the early spectra of SN 2023ufx. This can be translated into a constraint on the mass-loss rate at death of $\dot{M} \lesssim 10^{-3}\,M_{\odot}\,\mathrm{yr}^{-1}$ (e.g., L. Dessart et al. 2017; I. Boian & J. H. Groh 2019; W. V. Jacobson-Galán et al. 2024) due to the lack of any narrow H, He I, and He II in the spectra.

5.2. Photospheric Spectra

Days $\approx$ 20–40 are characterized by spectra typical of SNe II during the plateau phase, including a broad P Cygni Hα profile and absorption in the higher-order Balmer transitions. The photospheric spectra show minimal Hα absorption and above-average velocities, in agreement with other fast-evolving (short plateau and IIL) SNe II (e.g., C. P. Gutiérrez et al. 2014; D. Hiramatsu et al. 2021). Figure 6 shows the evolution of the Hα and Hβ features compared to the SN II sample of C. P. Gutiérrez et al. (2017a). Overall, the Hα and Hβ velocities of SN 2023ufx are slightly faster than normal SNe II during the plateau phase.

The starkest discrepancy with other SNe II is the nearly complete absence of any metallic absorption features. Figure 7 compares the high-quality MODS spectrum obtained +31 days after explosion to the Z-dependent model spectra of L. Dessart et al. (2013). The Fe II and Ca II features in SN 2023ufx are weaker than even the 0.1 $Z_{\odot}$ model spectrum at a similar phase.

We attempt two methods for deriving an upper limit on the pEW W_{λ} of Fe II λ5018 in the +31 day MODS spectrum. The first method is purely empirical and based upon Equation (4) from D. C. Leonard & A. V. Filippenko (2001),

$$W_{\lambda}(N\sigma) = N \times \Delta I \sqrt{W_{\mathrm{line}}\,\Delta X}, \quad (1)$$

for an $N\sigma$ limit where ΔI is the rms of the normalized continuum, W_{line} is the width of the spectral feature, and ΔX is the spectral bin size. For the MODS spectrum, $\Delta X = 2.5$ Å and we adopt $W_{\mathrm{line}} = 64$ Å corresponding to an Fe II velocity FWHM of 3000 km s^{-1}, slightly higher than the $\approx$2500 km s^{-1} FWHM measured for Fe II λ5018 at >60 days after explosion.

Fe II λ5018 sits atop the Hβ P Cygni profile so we must first remove its contribution to estimate ΔI. We fit a simple double-Gaussian model to the profile with one absorption component and one emission component, which decently replicate the observed profile, as shown in Figure 8. Normalizing by this continuum we find an $N\sigma$ upper limit on the Fe II λ5018 pEW of $W_{5018}(N\sigma) < N \times 0.4$ Å.

We also tried to fully model the Hβ P Cygni profile and Fe II $\lambda\lambda\lambda$4924, 5018, 5169 features using a Markov Chain Monte Carlo (MCMC) routine. This only converges if we fix the velocities of the Fe II features, otherwise the minimizer consistently prefers solutions with implausibly broad ($\Delta v > 10^4$ km s^{-1}) Fe II lines. The best-fit model has

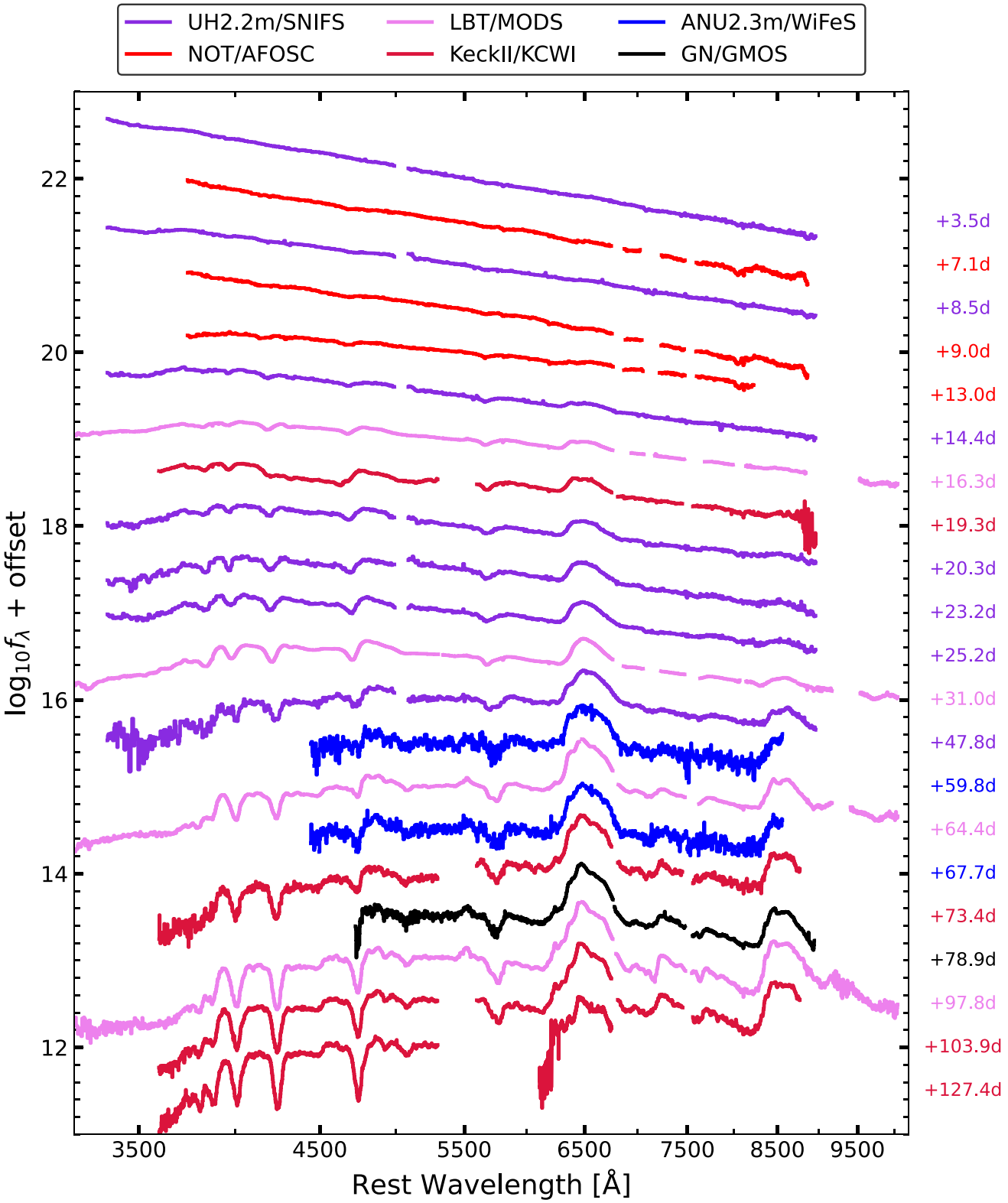

Figure 5. Optical spectra of SN 2023ufx, color coded by instrument and smoothed for visual clarity. Regions with significant telluric or instrumental artifacts are masked. Phases along the right axis are given relative to t_{exp} (Section 4.1). These spectra are available as the data behind the figure.
(The data used to create this figure are available in the online article.)

$W_{5018} = 2.2 \pm 1.9$ Å and it is included in Figure 8. The uncertainty is large due to the strong covariance between W_{5018} and the strength and width of the Hβ emission.

We adopt a conservative upper limit of $W_{5018} < 1.6$ Å for the +31 day spectrum, corresponding to an empirical 4σ limit, which qualitatively agrees with the MCMC results. This value is included in Figure 9 and confirms the metal-poor nature of SN 2023ufx. The low signal-to-noise ratio of the three spectra spanning 37–60 days precludes meaningful constraints on the Fe II features. For example, the 3σ upper limit on the pEW of

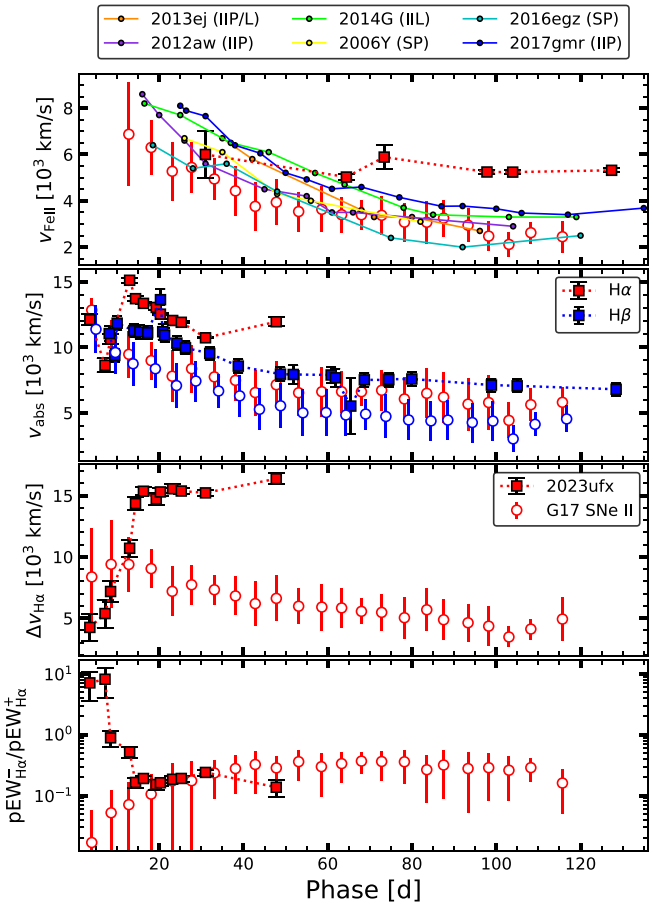

Figure 6. Fe II 5169 Å absorption velocity (top), Hα and Hβ absorption velocities (upper middle), Hα emission FWHM (lower middle), and the pseudo-equivalent width (pEW) ratio of Hα absorption over emission (bottom). The ensemble SN II results of C. P. Gutiérrez et al. (2017a, open circles) are shown in all panels for comparison and the Fe II λ5169 velocities for some well-studied SNe II are included in the top panel. References are provided in Table 5. The information is available as the data behind the figure.

(The data used to create this figure are available in the online article.)

Fe II λ5018 in the SNIFS +48 day spectrum from Equation (1) is ≈12 Å.

5.3. Late/Seminebular Spectra

The spectra ≳50 days after explosion show no evidence for Hα absorption, consistent with the light curve transitioning into the radioactive-decay phase. The Hα emission profiles develop an asymmetric, multipeaked structure with an FWHM velocity of $\approx 15 \times 10^3$ km s^{-1}. Figure 10 shows the evolution of the Hα profile. A distinct red component in the Hα profile appears between the +79 and +98 day spectra, which strengthens in the +127 day spectrum. The peak is at 6680 Å, near He I λ6678, but the double-peaked Paschen profiles (see below) suggest this is instead redshifted Hα moving at ∼5000 km s^{-1}. [O I] becomes visible and strengthens relative to Hα with time.

Fe II absorption finally appears at ≳60 days and thus must originate in the He layer, confirming that the H envelope was almost entirely devoid of Fe ions. But, as seen in Figure 11, the He-layer Fe II λ5018 features are significantly weaker than in other SNe II. In the absence of the metal blends at ≲4500 Å, Hγ and Hδ remain strong absorption features until the end of our campaign.

The lack of velocity evolution in Fe II λ5169 agrees with it originating in the He layer but the velocities measured from the absorption-line minima are anomalously high compared to the other SNe II in Figure 6. The high velocities are seen in multiple spectra with an excess of ≈2500 km s^{-1}. This will be discussed in Section 6.4.

Figure 12 shows the phase-matched optical and NIR spectra. The NIR Paschen features exhibit complex velocity structure. We overlay the Pβ and Pγ profiles with Hα in Figure 13. Inspecting the compilations of SN II NIR spectra published by S. Davis et al. (2019) and S. Tinyanont et al. (2024), we find no similarities with the NIR spectra of SN 2023ufx beyond the presence of Paschen emission lines.

The shapes of the double-peaked Pβ and Pγ profiles are broadly consistent with the Hα profile. Fitting the averaged Paschen profile with a double-Gaussian model we find velocity shifts $v_1 = -5700 \pm 900$ km s^{-1} and $v_2 = 3800 \pm 1200$ km s^{-1}. The widths are $\Delta v_1 = 6700 \pm 800$ km s^{-1} and $\Delta v_2 = 11{,}400 \pm 1600$ km s^{-1}. The ratio of blue to red flux is $f_{\rm b/r} = 0.63 \pm 0.13$. If we assume the blue and red components have similar velocities from a common origin (which may be incorrect), the two peaks are separated by ±4800 km s^{-1} from a bulk velocity of −1000 km s^{-1}.

We defer direct comparisons to the nebular spectra models of A. Jerkstrand et al. (2014) until we can obtain spectra deeper into the nebular phase. The early/seminebular spectra do show [O I], which is a diagnostic of the synthesized O mass, but the models are computed for ≳200 days after explosion when the densities are much lower than our observations of SN 2023ufx. Metallicity also likely plays a role in both the envelope and core emission properties given the distinct observational properties of SN 2023ufx outlined so far.

The clearest difference between SN 2023ufx and normal SNe II at these phases is the consistent presence of [O I] λ5577 in Figure 14. The ratio of [O I] λ5577 to λ6300 flux ($f_{5577/6300}$) constrains the density and temperature of the emitting material (e.g., P. Hartigan et al. 2004) with typical nebular SNe II exhibiting $f_{5577/6300} \sim 0.01$–0.1 (A. Jerkstrand et al. 2014). We measure the flux ratio in the three spectra that cover both features (GMOS + MODS) finding $f_{5577/6300} = 3.8 \pm 0.5$, 4.6 ± 0.9, and 2.0 ± 0.2 at +64, +79, and +98 days, respectively. [O I] λ5577 is seen in late-time spectra of SNe IIb (e.,g., A. Jerkstrand et al. 2015) such as SN 2011dh (e.g., I. Shivvers et al. 2013; M. Ergon et al. 2014) and $f_{5577/6300} > 1$ implies a hotter and denser He core than normal SNe II, again suggestive of a massive progenitor. The [O I] λλ6300, 6363 flux ratio is below the optically thin limit ($f_{6363/6300} = 1/3$) at <100 days, suggesting photon scattering in the H envelope is suppressing the redder component. The flux ratio rises to 0.8 ± 0.1 by +127 days, approaching the optically thick limit ($f = 1$) and closer to the expectations for the [O I] λλ6300, 6363 evolution (e.g., K. Maguire et al. 2012).

6. Discussion

6.1. A Glimpse at Type II Supernovae in the Early Universe

To highlight the uniqueness of SN 2023ufx's environment, we show the galaxy mass–metallicity plane in Figure 15. We use the luminosity–metallicity relation derived by D. A. Berg et al. (2012) specifically for low-luminosity galaxies. Using their fit to the combined + select sample and $M_B = -13.29 \pm 0.16$ mag from the SDSS photometry suggests

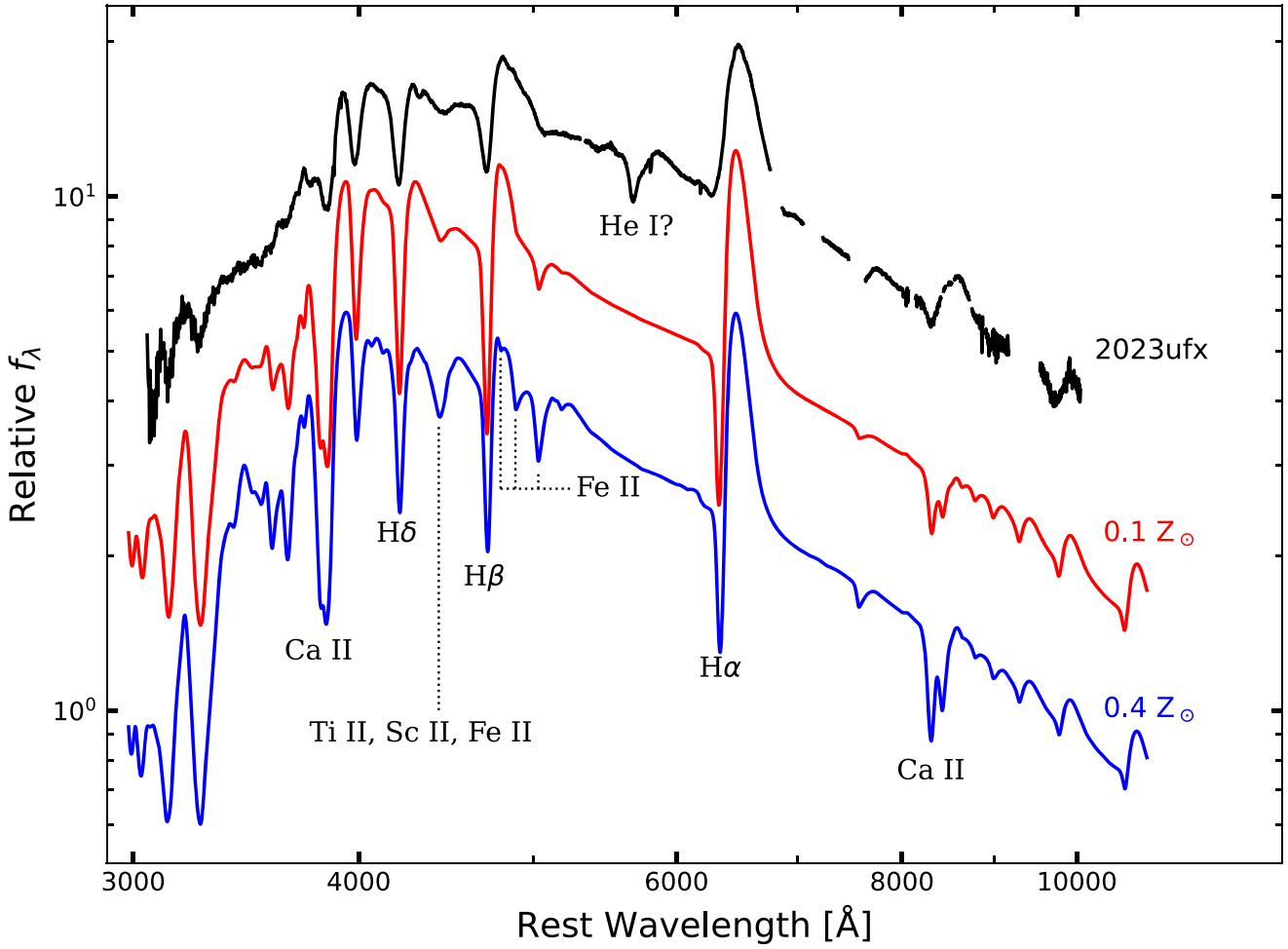

Figure 7. Comparison of the +31 day MODS spectrum with the 0.4 $Z_\odot$ (blue) and 0.1 $Z_\odot$ (red) model spectra from L. Dessart et al. (2013) at the same phase. Spectra are aligned to the Hβ blueshift of SN 2023ufx to ease visual comparisons. Important spectral features are marked.

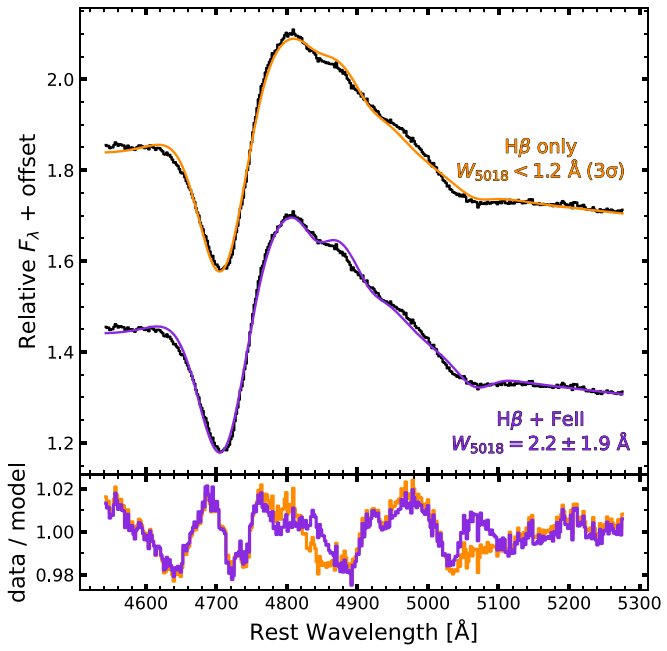

Figure 8. Comparison of two methods for estimating the Fe II λ5018 pEW in the high-quality +31 day MODS spectrum (Figure 7) discussed in Section 5.2. The residuals are shown in the lower panel following the same color scheme.

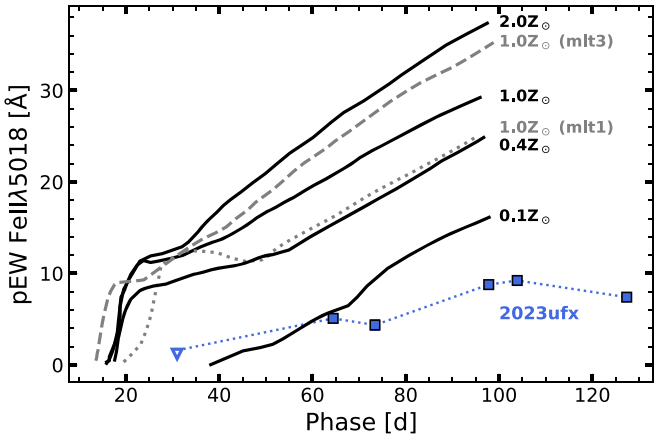

Figure 9. The evolution of the Fe II λ5018 pEW in SN 2023ufx (blue) compared to the models from L. Dessart et al. (2013) at different metallicities (black). Two solar-metallicity models with different mixing-length prescriptions during stellar evolution, also from L. Dessart et al. (2013), are shown in gray. The inverted triangle shows the pEW upper limit derived in Section 5.2 and shown in Figure 8.

$12 + \log_{10}(\mathrm{O/H}) = 7.73 \pm 0.25$ dex ($Z_{\rm host} \sim 0.1\ Z_\odot$). This value is shown in Figure 15.

For comparison we include galaxies from SDSS Data Release 8 (D. J. Eisenstein et al. 2011) and SN II hosts from

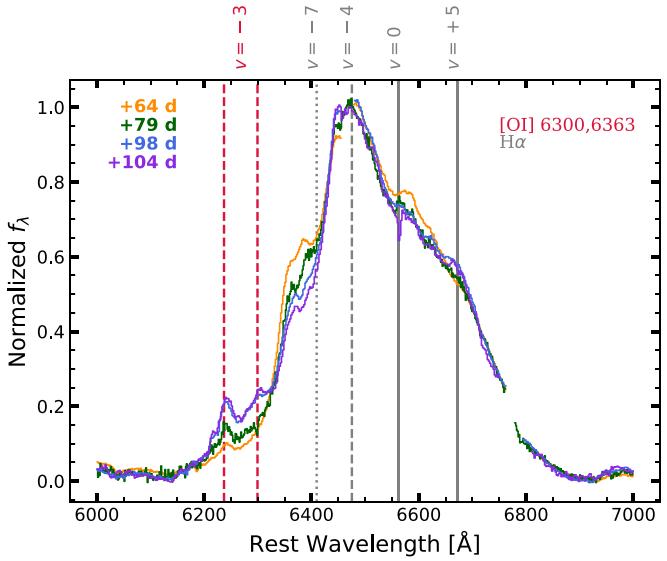

Figure 10. Normalized evolution of the Hα emission complex spanning ≈65–105 days after explosion. Phases for each spectrum are provided in the upper-left corner. [O I] appears at the onset of the radioactive-decay phase and strengthens with time. A redshifted Hα component appears in the last KCWI high-resolution spectrum—a comparison to the NIR spectra in Figure 13 confirms that this feature is not due to low-velocity He I λ6678. Labels along the top axis give velocities in 10^3 km s^{-1} for Hα (gray) and [O I] (red).

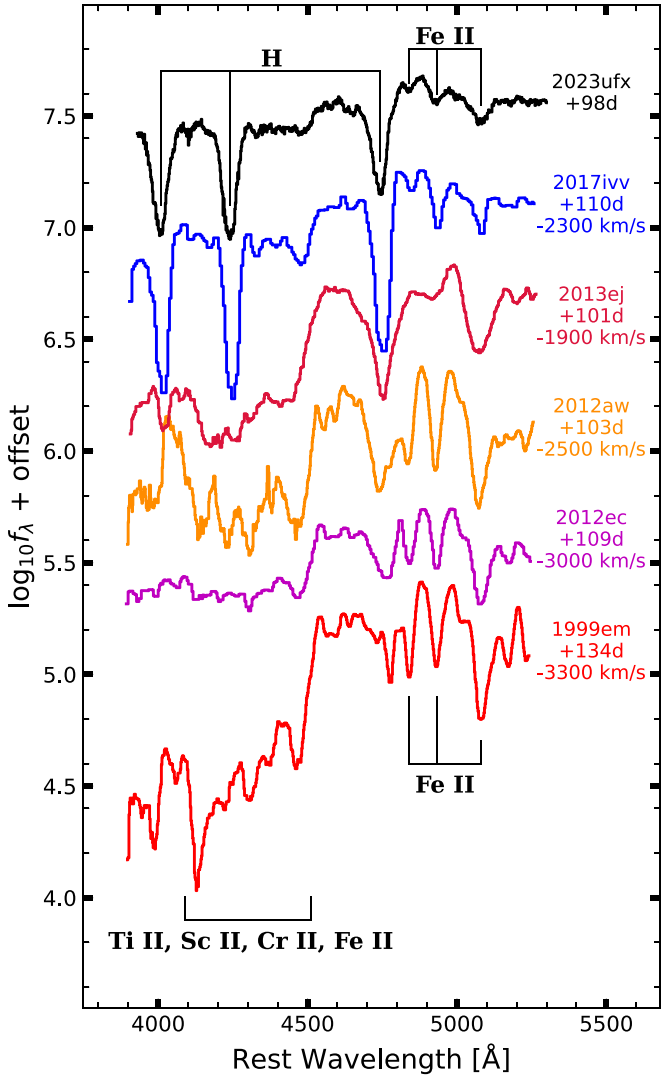

Figure 11. Comparing the high-quality +98 day spectrum to other SNe II in the literature. Each spectrum is aligned to Fe II λ5169 with the velocity offset given in each label. SN 2023ufx exhibits strong H absorption, weak Fe II features, and the blend of singly ionized metals from ≈4100 to 4500 Å is absent.

P. L. Kelly & R. P. Kirshner (2012), C. P. Gutiérrez et al. (2018), and K. Taggart & D. A. Perley (2021). SN metallicities are updated from J. F. Graham (2019), R. Ganss et al. (2022), and P. J. Pessi et al. (2023) where possible. We caution that oxygen abundance estimates for SNe II are heterogeneous, with local SNe II benefiting from local/environmental estimates from integral-field observations (e.g., H. Kuncarayakti et al. 2013, 2018; L. Galbany et al. 2016), whereas more distant sources must rely on integrated galaxy properties and luminosity–metallicity relations (e.g., I. Arcavi et al. 2010; N. E. Sanders et al. 2013). We also include the targeted dwarf galaxies from D. A. Berg et al. (2012) and T. Hsyu et al. (2018) and a sample of high-z galaxies from JWST with "direct" (T_e-based) oxygen abundances (M. Curti et al. 2023; K. E. Heintz et al. 2023; K. Nakajima et al. 2023; T. Morishita et al. 2024).

The combination of low host metallicity and the dearth of metal lines in the photospheric spectra (see Figures 7 and 11) implies $Z_{SN} < 0.1\ Z_\odot$. The iron in the envelopes of RSGs is primordial not nucleosynthetic so this low metallicity directly applies to the progenitor star. Only a handful of extremely metal-poor SNe II have been identified thus far. Besides SN 2023ufx, only SNe 2015bs (J. P. Anderson et al. 2018) and 2017ivv (C. P. Gutiérrez et al. 2020) are compelling cases for $Z_{SN} \lesssim 0.1\ Z_\odot$ exhibiting both weak Fe II features and extremely low host metallicities. The list of metal-weak ($Z \lesssim 0.5\ Z_\odot$) SNe II is growing (e.g., F. Taddia et al. 2016; A. Singh et al. 2018; K. A. Bostroem et al. 2019; C. P. Gutiérrez et al. 2020; X. Zhang et al. 2022), but the local scarcity of such environments inherently limits these opportunities.

6.2. Mass Loss: Stellar Winds or Binarity?

The short plateau requires a low M_{env} ($\sim 1\ M_\odot$, Section 4.2), which is difficult to reconcile with typical RSG evolution producing $\gtrsim 5\ M_\odot$ H envelopes and ∼80–150 day plateaus (e.g., T. Sukhbold et al. 2016; B. L. Barker et al. 2022). The two mechanisms for removing several solar masses from the envelope prior to collapse are strong, possibly eruptive, stellar winds or stripping by a nearby companion.

Conventional stellar-wind prescriptions (e.g., C. de Jager et al. 1988; J. S. Vink et al. 2001) depend on metallicity as $\dot{M} \propto Z^\alpha$ where $\alpha = 0.3$–0.8 (e.g., J. S. Vink 2022) so stellar winds should be 10%–50% weaker for the progenitor of SN 2023ufx than for a star at solar metallicity. Weakened stellar winds at low Z should increase the fraction of massive stars that retain some of their H envelope at death (i.e., the N_{II}/N_{Ibc} ratio; e.g., E. R. Stanway et al. 2020). Thus, a massive star that would have exploded as a SN Ib or IIb in a luminous metal-enriched galaxy may instead produce a short-plateau SN II–like SN 2023ufx.

An initially massive progenitor for SN 2023ufx agrees with the above-average $M_{Ni} \sim 0.1\ M_\odot$ estimated in Section 4.3 and the detection of [O I] λ5577 (Section 5.3). Yet this requires some fine-tuning to produce SN 2023ufx as the star must be massive enough to partially strip the envelope but not so

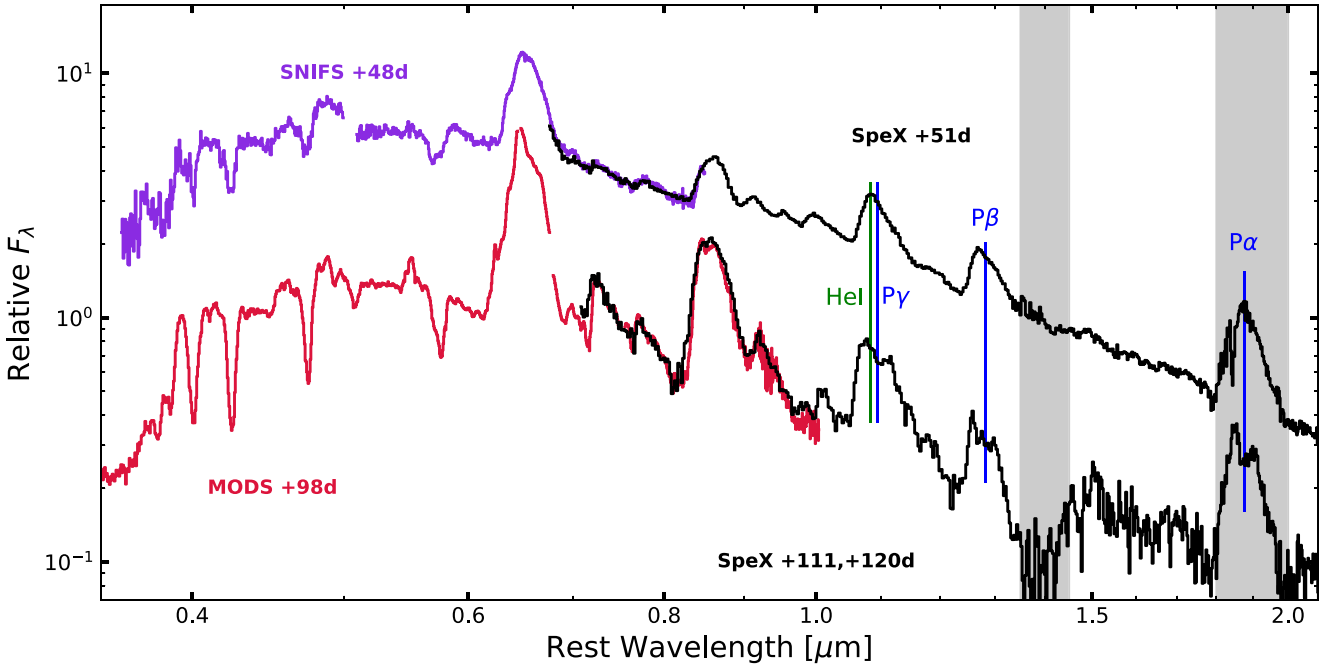

Figure 12. NIR spectra of SN 2023ufx from SpeX (+51 days and ≈+115 days, black) shown alongside contemporaneous optical spectra from SNIFS (+48 days, purple) and MODS (+98 days, red). The Pα, Pβ, Pγ, and He I 1.083 μm features are marked with vertical colored lines. Regions with significant telluric absorption are shaded gray.

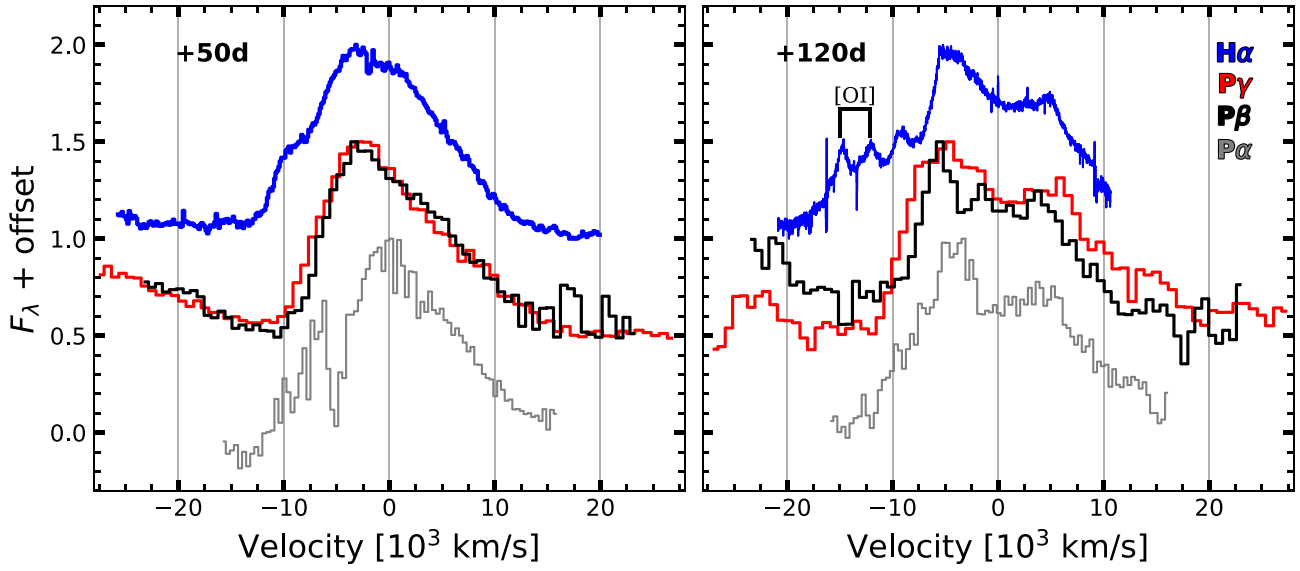

Figure 13. Comparison of the Hα and Paschen profiles at ≈+50 days (left) and ≈120 days (right). While the Pα line falls in a strong telluric region, its structure is similar to the Pβ and Pγ profiles. The +50 day profiles are single-peaked whereas the +120 day profiles are distinctly double peaked.

massive as to remove it entirely. Given that SN 2023ufx is just the third SN II with extremely low metallicity, such a fine-tuned scenario seems implausible but is not strictly impossible.

The lack of narrow emission features in the early spectra of SN 2023ufx restrict the mass-loss rate at death to $<10^{-3}\,M_\odot\,\mathrm{yr}^{-1}$ (Section 5.1), which disallows large outbursts or eruptions leading up to collapse. It does not exclude enhanced winds during the main-sequence phase, and Section 6.4 outlines evidence for enhanced rotation in the progenitor of SN 2023ufx. Turbulent motions in the envelope can boost wind mass-loss rates by orders of magnitude (e.g., N. D. Kee et al. 2021) and rotation-induced turbulence can also dredge up metals from the core into the envelope to increase wind-driven mass loss (e.g., N. Markova et al. 2018). However, the low Fe abundance in the photospheric phase requires minimal metals in the RSG envelope and excludes strong mixing during the explosion. Theoretical studies are needed to fully capture the connections between turbulence, rotation, and stellar winds at low Z.

Binary interaction is the other mechanism for removing several solar masses from the envelope. Stripping from a nearby companion is commonly invoked to explain the sequence of partially stripped SNe II (e.g., T. J. Moriya et al. 2016; L. Dessart et al. 2024) and can explain the observed occurrence rates (e.g., J. J. Eldridge et al. 2018). The primary argument against binarity producing partially or fully stripped CC SNe is the dearth of identified companions. Massive stars have massive companions

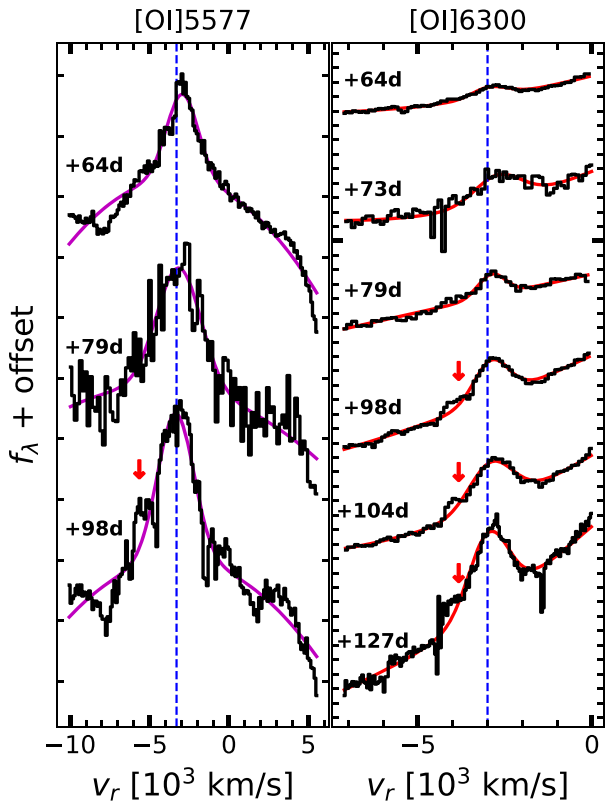

Figure 14. Evolution of the [O I] λ5577 and [O I] λ6300 emission lines at ≈65–130 days after explosion. Blue dashed lines show the average velocity shift of each line, $v_{5577} \approx -3300$ km s^{-1} and $v_{6300} \approx -3000$ km s^{-1}. The [O I] λ5577 line is twice as broad (≈2600 km s^{-1}) compared to the [O I] λ6300 emission (≈1300 km s^{-1}). Red arrows denote potential high-velocity features.

(e.g., H. Sana et al. 2012) and most will experience mass transfer or interaction over the course of stellar evolution (e.g., H. A. Kobulnicky & C. L. Fryer 2007). The list of SNe II with identified progenitors has steadily grown (e.g., S. J. Smartt et al. 2004; J. R. Maund et al. 2013, 2014; M. Fraser 2016) yet no binary companions have been identified in a canonical SN II, fast-evolving or otherwise (e.g., S. D. Van Dyk et al. 2023). Tentative companions have been identified for some SNe IIb (J. R. Maund et al. 2004, 2015; S. D. Ryder et al. 2018), but the Galactic SN IIb Cas A has strict limits on a companion (e.g., C. S. Kochanek 2018; W. E. Kerzendorf et al. 2019) and most recent Galactic CC SNe did not have a companion at the time of explosion (C. S. Kochanek 2021, 2023).

This lack of detected companions is difficult to reconcile with the high O/B binarity fraction of ∼70% and subsequent 30% binary fraction of their RSG descendants (e.g., K. F. Neugent et al. 2020; K. F. Neugent 2021). The flat mass-ratio and orbital-period distributions of massive-star binaries (e.g., T. Shenar et al. 2022) also disfavor low-mass companions to all SNe II with detected progenitors. If short-plateau SNe II are truly the result of partial stripping from a nearby companion, there are enough SNe IIP with progenitor detections (e.g., Ó. Rodríguez 2022) that a distant (i.e., noninteracting) and massive (mass ratio $q \gtrsim 0.8$) companion could be present in at least one nearby SN II.

6.3. Circumstellar Medium Interaction

While the lack of narrow features in the early spectra (Section 5.1) excludes optically thick CSM near the progenitor's surface, it does not probe extended optically thin CSM that contributes a blue continuum to the observed fluxes. This CSM configuration explains the SNe II with above-average luminosities, weak absorption features, and broad emission lines (e.g., P. J. Pessi et al. 2023). Moreover, all SNe II should become interaction dominated at some point in their evolution (e.g., L. Dessart & D. J. Hillier 2022), which is seen in local CC SNe (e.g., D. Milisavljevic et al. 2012; M. Rizzo Smith et al. 2023).

CSM interaction could explain the above-average peak luminosity and boxy Hα and [O I] profiles seen in the late-time spectra. Yet the CSM interaction models of L. Dessart & D. J. Hillier (2022) predict UV emission commensurate with shock interaction power. The weakest shock power considered by L. Dessart & D. J. Hillier (2022) of 10^{40} erg s^{-1} predicts an early Swift *UVW2* magnitude of −14 mag, brighter than the latest Swift observations in Figure 2. CSM interaction could have started at later times but the interaction models consistently predict a blue continuum which is not seen in the spectra of SN 2023ufx extending to $\lesssim$3500 Å (see Figures 7 and 12).

Weaker CSM interaction could be present but it appears unlikely to explain the lack of metal features in SN 2023ufx or the double-peaked Paschen lines. The dilution of spectral features by CSM interaction cannot explain the late-time Hδ and Hγ features in Figure 11, which are replaced by metal species in other SNe. We will continue monitoring SN 2023ufx as it progresses through the nebular phase to better understand the preexplosion circumstellar environment.

6.4. Linking Metallicity, Rotation, and Feedback

The most plausible explanation for the high Hα, [O I], and Fe II λ5169 velocities is an inherently aspherical explosion (e.g., A. Wongwathanarat et al. 2013, 2015; S. M. Couch & C. D. Ott 2015), possibly oriented along our line of sight. The velocities are an order of magnitude (or more) too high to attribute the explosion to unbinding a binary or neutron star/black hole kicks (e.g., D. Sweeney et al. 2022). Radiative transfer and photon scattering in partially nebular ejecta can produce blueshifted emission features even when the underlying emitting material has zero net velocity (e.g., A. Jerkstrand 2017). However, this should produce a distinctive evolution back to the rest velocity of the emitting material as the optical depth diminishes, which is not observed.

There is ample evidence that most (or all) CC explosions are inherently aspherical at some level (e.g., K. Kifonidis et al. 2003; P. A. Mazzali et al. 2005; K. Maeda et al. 2008; S. M. Couch et al. 2009; L. A. Lopez et al. 2009; R. Chornock et al. 2010; A. Wongwathanarat et al. 2013), but faster rotation may increase asymmetries at low metallicities (e.g., A. Maeder & G. Meynet 2000; S. E. Woosley & J. S. Bloom 2006; Z. Cano et al. 2017). Stellar winds exert a torque on the star by interacting with the magnetic field (magnetic braking; e.g., Z. Keszthelyi et al. 2022) and reduce the rotation rate. Weaker stellar winds at lower metallicity will decrease angular momentum losses (e.g., N. Yusof et al. 2013; A. Maeder & G. Meynet 2014), leading to rapidly rotating progenitors with more energetic explosions (e.g., S. M. Couch et al. 2009; O. Papish & N. Soker 2011; P. Mösta et al. 2015).

This connection between rotation and metallicity is seen in the environmental properties of the Type Ic SNe (SNe Ic) originating from massive stars that have lost their H and He

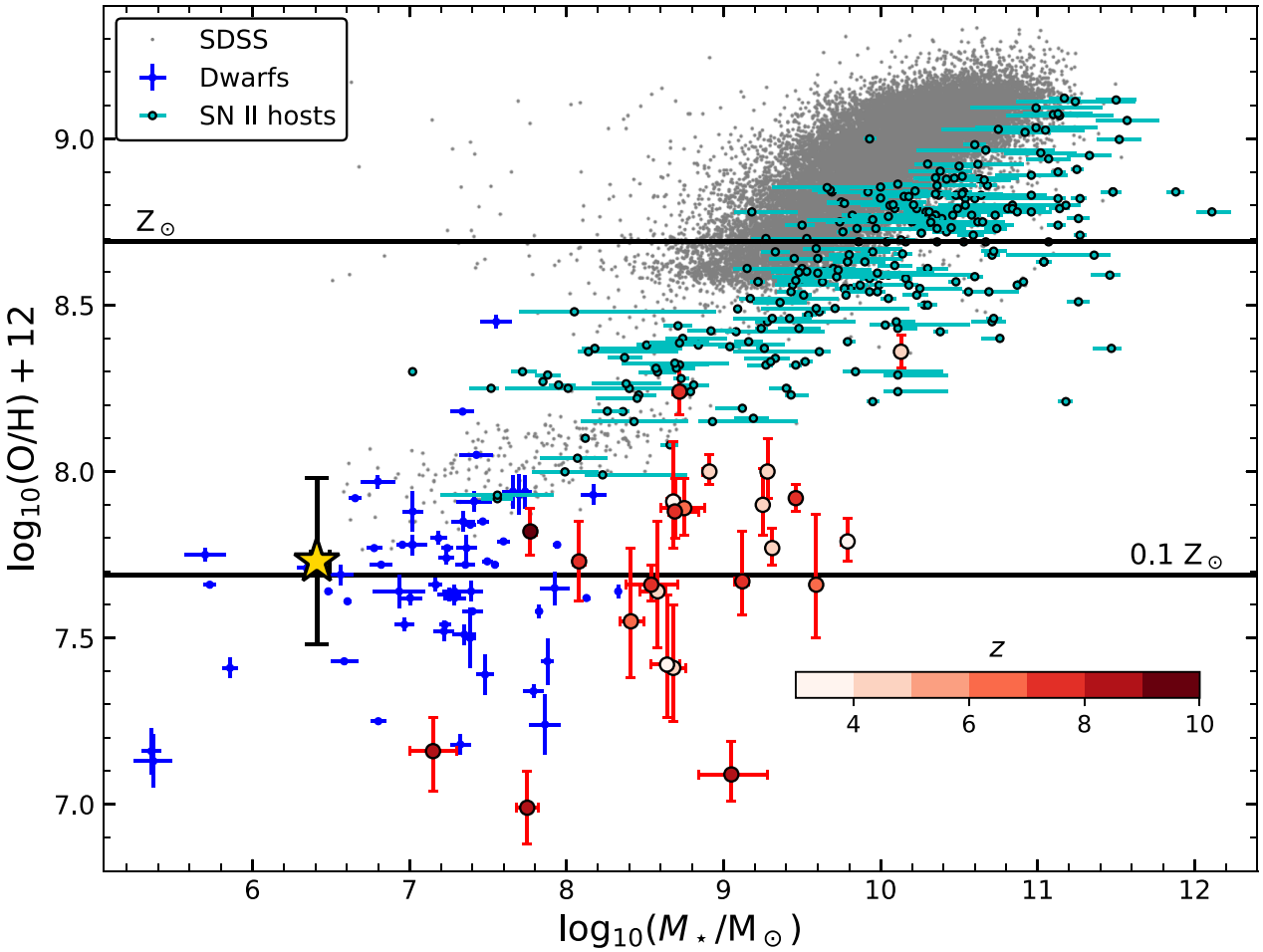

Figure 15. The galaxy mass–metallicity plane discussed in Section 6.1. We compare the host galaxy of SN 2023ufx (gold star) to SDSS (gray points, D. J. Eisenstein et al. 2011), local dwarfs (dark blue points, D. A. Berg et al. 2012; T. Hsyu et al. 2018), SN II hosts (light blue points, P. L. Kelly & R. P. Kirshner 2012; C. P. Gutiérrez et al. 2018; K. Taggart & D. A. Perley 2021), and high-redshift galaxies from JWST (M. Curti et al. 2023; K. E. Heintz et al. 2023; K. Nakajima et al. 2023; T. Morishita et al. 2024) with the redshift given by the red color bar.

layers. Normal SNe Ic prefer environments with enhanced (supersolar) metallicity (e.g., M. Modjaz et al. 2011, 2020), but the energetic broad-lined SNe Ic(-BL) associated with long γ-ray bursts and relativistic jets (e.g., L. Izzo et al. 2019) occur almost exclusively in metal-poor dwarf galaxies (e.g., K. M. Svensson et al. 2010; T. Krühler et al. 2015). From a purely statistical view, normal and broad-lined SNe Ic may originate from completely independent stellar populations (e.g., A. S. Fruchter et al. 2006; M. Modjaz et al. 2020).

The one other SN II with a robust metallicity of $\lesssim 0.1\ Z_\odot$, SN 2015bs (J. P. Anderson et al. 2018), appears to be a less extreme version of SN 2023ufx. SN 2015bs was more luminous than local SNe II, exhibited fast ejecta velocities, and had a slightly shorter plateau than the median for SNe II (e.g., J. P. Anderson et al. 2014; S. Valenti et al. 2016). If the photometric and spectroscopic properties of local SNe II (J. P. Anderson et al. 2014; S. Valenti et al. 2016; C. P. Gutiérrez et al. 2017a, 2017b) are representative of all SNe II, the binomial probability of the first two metal-poor SNe II consistently exhibiting all three of these properties is $<1\%$.

This also implies metallicity-dependent feedback from CC SNe because of the increased ejecta velocities and prevalence for outflows and jets. Nucleosynthetic yields also depend on progenitor metallicity due to the core electron fraction increasing with metallicity from partially and fully ionized metals. Thus, cosmological simulations must account for changes in CC SN feedback across cosmic time. The same metals ejected by early SNe II will affect the evolution and explosion of subsequent massive stars.

7. Summary

We presented extensive optical and NIR observations of the peculiar SN II 2023ufx. It exploded in the outskirts of a metal-poor ($Z_{\rm host} \sim 0.1\ Z_\odot$) dwarf galaxy ($M_\star \sim 10^{6.4}\ M_\odot$). SN 2023ufx provides a glimpse into the death of massive stars at low Z expected in the early Universe. The plateau phase is short ($\sim$20 days) indicating a thin ($\sim 1\ M_\odot$) H envelope. The complete lack of Fe II in the plateau-phase spectra confirm a progenitor with $Z_\star \lesssim 0.1\ Z_\odot$. We measure $M_{\rm Ni} \sim 0.1\ M_\odot$ from the late-time light curve, which suggests a massive progenitor. The late-time H emission lines are bimodal, which we attribute to fast outflows ($\sim$5000 km s^{-1}) launched during the explosion, possibly due to a rapidly rotating progenitor.

The combination of low metallicity and fast evolution make SN 2023ufx a probe of massive-star evolution in the low-Z early Universe. If the nebular spectra confirm a massive progenitor, SN 2023ufx is evidence for a higher fraction of SNe II at lower metallicities and high redshifts due to weakened stellar winds. Finding fast outflows in one of the

two known SNe II at such low metallicities suggests a connection to the rapidly rotating progenitors of SNe Ic-BL and γ-ray bursts.

Acknowledgments

We thank Michelle Tucker, Todd Thompson, and Kris Stanek for useful discussions. We thank Rick Pogge and Paul Martini for discussions about galaxy metallicity estimates and their reliability.

Parts of this research were supported by the Australian Research Council Discovery Early Career Researcher Award (DECRA) through project number DE230101069.

C.A. acknowledges support by NASA grants JWST-GO-02114, JWST-GO-02122, JWST-GO-03726, JWST-GO-04436, and JWST-GO-04522.

This material is based upon work supported by the National Science Foundation Graduate Research Fellowship Program under grant Nos. 1842402 and 2236415. Any opinions, findings, and conclusions or recommendations expressed in this material are those of the author(s) and do not necessarily reflect the views of the National Science Foundation.

M.N. is supported by the European Research Council (ERC) under the European Unions Horizon 2020 research and innovation program (grant agreement No. 948381) and by UK Space Agency grant No. ST/Y000692/1.

M.P. acknowledges support from a UK Research and Innovation Fellowship (MR/T020784/1).

This work is based on observations made with the Large Binocular Telescope. The LBT is an international collaboration among institutions in the United States, Italy, and Germany. LBT Corporation partners are: the University of Arizona on behalf of the Arizona Board of Regents; Istituto Nazionale di Astrofisica, Italy; LBT Beteiligungsgesellschaft, Germany, representing the Max-Planck Society, the Leibniz Institute for Astrophysics Potsdam, and Heidelberg University; the Ohio State University, representing OSU, University of Notre Dame, University of Minnesota, and University of Virginia.

This paper used data obtained with the MODS spectrographs built with funding from NSF grant AST-9987045 and the NSF Telescope System Instrumentation Program (TSIP), with additional funds from the Ohio Board of Regents and the Ohio State University Office of Research.

Pan-STARRS is a project of the Institute for Astronomy of the University of Hawaii, and is supported by the NASA SSO Near Earth Observation Program under grants 80NSSC18K0971, NNX14AM74G, NNX12AR65G, NNX13AQ47G, NNX08AR22G, and 80NSSC21K1572, and by the State of Hawaii.

The Pan-STARRS1 Surveys (PS1) and the PS1 public science archive have been made possible through contributions by the Institute for Astronomy, the University of Hawaii, the Pan-STARRS Project Office, the Max-Planck Society and its participating institutes, the Max Planck Institute for Astronomy, Heidelberg and the Max Planck Institute for Extraterrestrial Physics, Garching, The Johns Hopkins University, Durham University, the University of Edinburgh, the Queen's University Belfast, the Harvard-Smithsonian Center for Astrophysics, the Las Cumbres Observatory Global Telescope Network Incorporated, the National Central University of Taiwan, the Space Telescope Science Institute, the National Aeronautics and Space Administration under grant No. NNX08AR22G issued through the Planetary Science Division of the NASA Science Mission Directorate, the National Science Foundation grant No. AST-1238877, the University of Maryland, Eotvos Lorand University (ELTE), the Los Alamos National Laboratory, and the Gordon and Betty Moore Foundation.

This paper used data obtained with the Infrared Telescope Facility, which is operated by the University of Hawaii under contract 80HQTR19D0030 with the National Aeronautics and Space Administration.

Based on observations made with the Nordic Optical Telescope, owned in collaboration by the University of Turku and Aarhus University, and operated jointly by Aarhus University, the University of Turku and the University of Oslo, representing Denmark, Finland and Norway, the University of Iceland, and Stockholm University at the Observatorio del Roque de los Muchachos, La Palma, Spain, of the Instituto de Astrofisica de Canarias. The data presented here were obtained in part with ALFOSC, which is provided by the Instituto de Astrofisica de Andalucia (IAA) under a joint agreement with the University of Copenhagen and NOT.

The automation of the ANU2.3 m telescope was made possible through an initial grant provided by the Centre of Gravitational Astrophysics and the Research School of Astronomy and Astrophysics at the Australian National University and partially through a grant provided by the Australian Research Council through LE230100063.

Facilities: UH:2.2m (SNIFS), NOT (ALOFC), Keck:II (KCWI), IRTF (SpeX), LBT (MODS), and ANU2.3m (ATT).

Software: astropy (Astropy Collaboration et al. 2013, 2018, 2022), matplotlib (T. A. Caswell et al. 2022), lmfit (M. Newville et al. 2021), spectres (A. C. Carnall 2017), numpy (S. van der Walt et al. 2011), pandas (The pandas development Team 2024), extinction (K. Barbary 2016), scipy (P. Virtanen et al. 2020), and astro-scrappy (C. McCully & M. Tewes 2019).

Appendix A
Data Reduction and Calibration

A.1. Photometry

We provide the light curves for SN 2023ufx from the ATLAS (*c* and *o*), ASAS-SN (*g*), ZTF (*g* and *r*), and Pan-STARRS (*g*, *r*, *i*, *z*, and *y*) surveys as supplementary material. Additional photometry was obtained with the Neil Gehrels Swift Observatory using the UVOT and the LBT MODS (R. W. Pogge et al. 2010).

For most of the Swift epochs, SN 2023ufx was observed with all six UVOT filters (T. S. Poole et al. 2008): *V* (5425.3 Å), *B* (4349.6 Å), *U* (3467.1 Å), *UVW*1 (2580.8 Å), *UVM*2 (2246.4 Å), and *UVW*2 (2054.6 Å). Most UVOT epochs contain at least two observations per filter, which we combined into one image for each filter using the HEASoft `uvotimsum` package. We used the `uvotsource` package to extract source counts using a 5.″0 radius region centered on the position of the SN and background counts using a source-free region with radius of 50.″0. We then converted the UVOT count rates into fluxes and magnitudes using the calibrations of T. S. Poole et al. (2008) and A. A. Breeveld et al. (2010; also see https://www.swift.ac.uk/analysis/uvot/). No host-galaxy flux is subtracted from the Swift photometry because we lack preexplosion and late-time imaging but this is mitigated by the faintness of the host.

LBT/MODS photometry was obtained in the *ugri* filters, which are analogous to the Sloan filter set. Images were

Table 4
Information for the Spectroscopic Observations

Tel./Instr.	MJD	Phase (days)	Range	$\lambda/\delta\lambda$	Notes
UH2.2m/SNIFS	60226.60	3.5	3400–9000 Å	1200	⋯
NOT/AFOSC	60230.25	7.1	3700–8800 Å	360	Grism 4, 1″ slit
UH2.2m/SNIFS	60231.59	8.5	3400–9000 Å	1200	⋯
NOT/AFOSC	60232.16	9.0	3700–8800 Å	360	Grism 4, 1″ slit
NOT/AFOSC	60236.18	13.0	3800–8200 Å	360	Grism 4, 1″ slit
UH2.2m/SNIFS	60237.60	14.4	3400–9000 Å	1200	⋯
LBT/MODS	60239.50	16.3	3100–10000 Å	2000	⋯
Keck II/KCWI	60242.59	19.3	3500–8700 Å	1800, 1000	BL + RL gratings
UH2.2m/SNIFS	60243.59	20.3	3400–9000 Å	1200	⋯
UH2.2m/SNIFS	60246.54	23.2	3400–9000 Å	1200	⋯
UH2.2m/SNIFS	60248.61	25.2	3400–9000 Å	1200	⋯
LBT/MODS	60254.45	31.0	3100–10000 Å	2000	⋯
UH2.2m/SNIFS	60271.48	47.8	3400–9000 Å	1200	⋯
IRTF/SpeX	60274.49	50.7	0.7–2.5 μm	100	⋯
UH2.2m/SNIFS	60274.57	50.8	3400–9000 Å	1200	⋯
ANU2.3m/WiFeS	60283.69	59.8	4500–8500 Å	3000	B + *R*3000 gratings
LBT/MODS	60288.41	64.4	3100–10000 Å	2000	⋯
ANU2.3 m/WiFeS	60291.68	67.7	4500–8500 Å	3000	B + *R*3000 gratings
Keck II/KCWI	60297.51	73.4	3500–8800 Å	1800, 1000	BL + RL gratings
GN/GMOS	60303.11	78.9	4700–8900 Å	2000	*R*400 grating, *G*5305 filter
LBT/MODS	60322.27	97.8	3100–10000 Å	2000	⋯
Keck II/KCWI	60328.47	103.9	3500–8700 Å	1800, 1000	BL + RL gratings
IRTF/SpeX	60335.46	110.8	0.7–2.5 μm	100	⋯
IRTF/SpeX	60344.43	119.6	0.7–2.5μm	100	⋯
Keck II/KCWI	60352.31	127.4	3600–6800 Å	1800, 6500	BL + RH2 gratings

Note. Phases are given in rest-frame days. Range gives the wavelength coverage of the spectrum in units of Å(optical) or μm (NIR), although see Figure 5 for gaps in the wavelength coverage for specific spectra. The approximate spectral resolution ($\lambda/\Delta\lambda$) is provided for each observation. KCWI observations have two entries for spectral range and resolution corresponding to the blue and red channels (see Appendix A).

calibrated with typical procedures including bias subtraction, dark subtraction, and flat-field corrections. The world coordinates solution was improved with the ASTROMETRY.NET software (D. Lang et al. 2010) and the photometry was calibrated using the REFCAT catalog (J. L. Tonry et al. 2018a). No host-galaxy subtraction is applied.

A.2. Spectroscopy

We obtained 24 epochs of optical spectroscopy (Figure 5) and three epochs of NIR spectroscopy (Figure 12) using a multitude of telescopes and instruments. We briefly describe the individual data processing procedures below. The full log of spectra is provided in Table 4.

UH2.2m + SNIFS. Eight spectra were obtained with the UH2.2m telescope using SNIFS (B. Lantz et al. 2004) and SCAT (M. A. Tucker et al. 2022). SNIFS covers the full optical range (≈3500–9000 Å) at modest resolution ($R \sim 1200$). Data reduction and calibration procedures are described by M. A. Tucker et al. (2022). The dichroic crossover region (≈5000–5200 Å) is affected by changes in humidity so nights with poor corrections have these regions masked.

NOT + ALOFC. The three spectra from ALFOSC on the NOT were all obtained with Grism 4 using a 1″ slit and 600 s exposures with no blocking filter under program P68-007. All spectra were reduced using the `PyNOT-redux` reduction pipeline.[20]

LBT + MODS. Three spectra were obtained with MODS (R. W. Pogge et al. 2010) on the LBT. The data were reduced with PYPEIT (J. Prochaska et al. 2020) producing four spectra per epoch, one blue and one red channel per instrument (MODS1/2). These were then combined to produce the final spectra using weighted averages and sigma clipping to remove outliers.

Keck II + KCWI. Four epochs of spectroscopy were obtained with the KCWI (P. Morrissey et al. 2018) on the Keck II telescope. The 2D images were reduced using PYPEIT (J. Prochaska et al. 2020), using typical procedures such as bias subtraction, flat-fielding, and wavelength calibration using the FeAr arc lamps. Data cubes were created from these 2D images using the subpixel method within PYPEIT_COADD_DATACUBE. The individual cubes were flux calibrated using a standard star observed on the same night. KCWI is an integral-field unit so we extract spectra from the cubes by fitting analytic profiles to each slice of the 3D cube. The 2D extraction assumes a circular Gaussian profile for the seeing and a spatially flat sky background for each slice in the 3D (x, y, λ) data cube. After extracting the 3D cube into 1D spectra the individual exposures are combined using sigma-clipped weighted averages to produce the final spectra.

The host galaxy becomes visible as SN 2023ufx fades. We simultaneously extracted host and source spectra by fitting two Gaussian profiles plus a spatially uniform sky background using the coordinate offsets. The shape parameters of the galaxy are determined by initially fitting a slice of the 3D cube centered on bright emission lines (typically Hα for the red

[20] github.com/jkrogager/PyNOT/

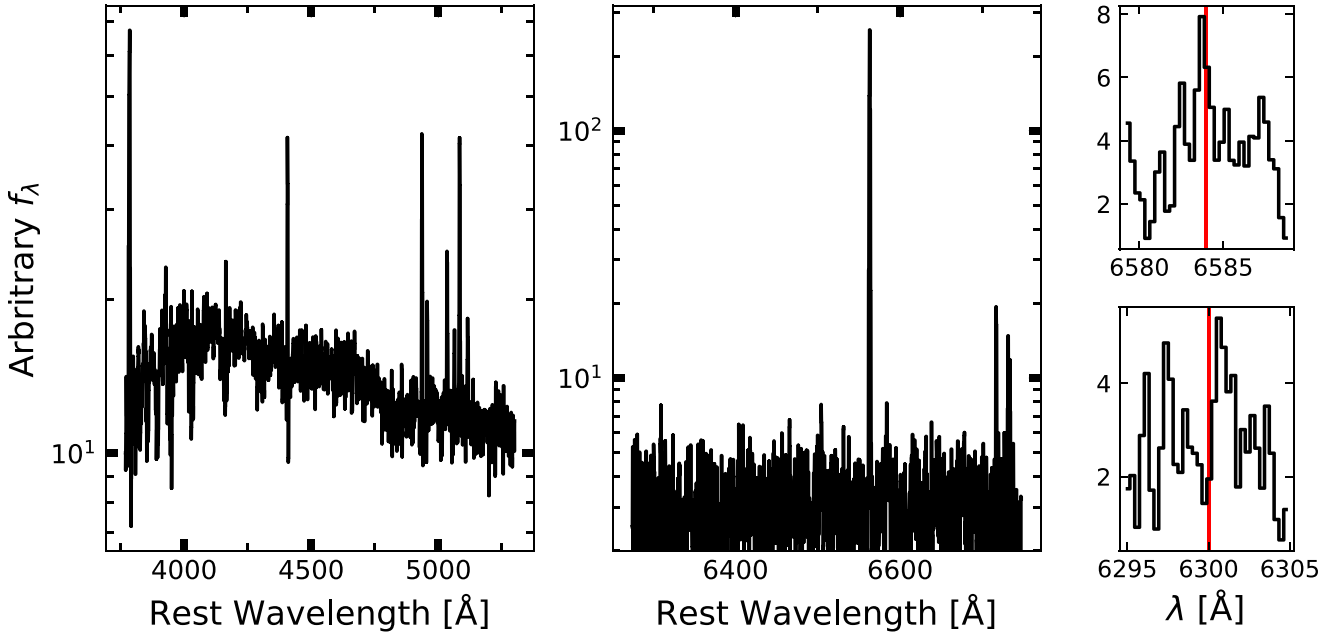

Figure 16. Host-galaxy spectrum extracted from the last KCWI observations. The small right panels shows insets around [N II] λ6584 (top, marginally detected) and [O I] λ6300 (undetected).

channel and [O II] λ3727 for the blue). Then, the shape and orientation are held fixed when measuring the integrated flux of each component as a function of wavelength in the 3D cube. Finally, the individual 1D spectra are combined to produce the final spectra shown in Figure 16.

ANU2.3m + WiFeS. Four spectra were obtained using WiFeS mounted on the ANU2.3m telescope located at Siding Spring Observatory (M. Dopita et al. 2007, 2010). Each spectrum was taken in "nod and shuffle" mode using the $R = 3000$ grating to cover the full 3000–9000 Å wavelength range. Each spectrum was reduced using PyWiFeS (version 0.7.4; M. J. Childress et al. 2014), with sky subtraction done using a 2D sky spectrum that was taken during the observations. See A. Carr et al. (2024) for more details. To increase the signal-to-noise ratio of these spectra, we merged these four spectra into two which are used in the analysis.

GN + GMOS. One spectrum is from GMOS (I. M. Hook et al. 2004) on the GN telescope. The spectrum used the *R*400 grating, the *G*5305 order-blocking filter, a 0.″5 wide slit, and 2×2 binning. The observations were reduced and extracted with PYPEIT (J. Prochaska et al. 2020).

IRTF + SpeX. Three epochs of NIR spectroscopy were obtained using SpeX (J. T. Rayner et al. 2003) on the NASA IRTF. The spectra were obtained in prism mode at a low spectral resolution of $R \sim 100$. We reduced these spectra with Spextool (M. C. Cushing et al. 2004) using flat and arc lamps taken immediately after the science spectra and then flux calibrated the extracted 1D spectra using nearby A0 telluric standard stars within a typical airmass difference of ≈0.01.

Appendix B
Additional Figures and Tables

Here we include additional figures and tables. Figure 16 shows the extracted host-galaxy spectrum from the latest KCWI observations. Figure 17 shows the preexplosion survey light curve. Figure 18 shows the photometric data used to infer t_{exp}. Figure 19 compares the *g*-band light curve of SN 2023ufx with the sample of S. Valenti et al. (2016).

Table 5 includes references for the comparison SNe II used throughout the analysis. Comparison SNe II were chosen to include well-studied canonical SNe IIP (SNe 1999em, 2012aw, 2012ec, and 2017eaw), SNe IIL (SNe 2013ej and 2014G) and short-plateau SNe II (SNe 2006ai, 2006Y, and 2016egz). SNe 2017gmr and 2017ivv were included because they share high absorption velocities and low host-galaxy metallicities, respectively, with SN 2023ufx. Most data are obtained from either the Weizmann Interactive Supernova Data Repository (O. Yaron & A. Gal-Yam 2012) or the Open Supernova Catalog (J. Guillochon et al. 2017).

The photometry (Figure 2) and spectroscopy (Figure 5) of SN 2023ufx are included in the online version of the manuscript. The measurements from Figure 6 are also included as the data behind the figure.

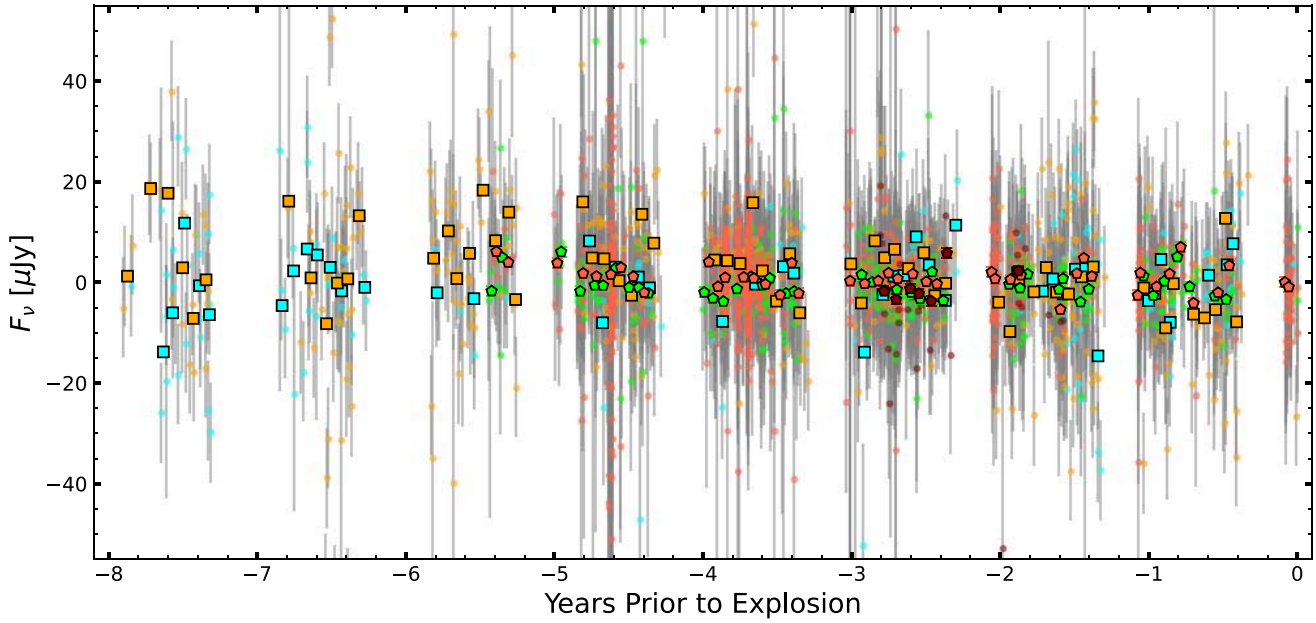

Figure 17. Preexplosion survey photometry from ZTF and ATLAS showing no outbursts or variability in the 8 yr preceding explosion. Single-night photometry is shown as small points with gray uncertainties whereas 30 day binned photometry is represented with larger bold points. Marker colors and symbols are the same as Figure 2.

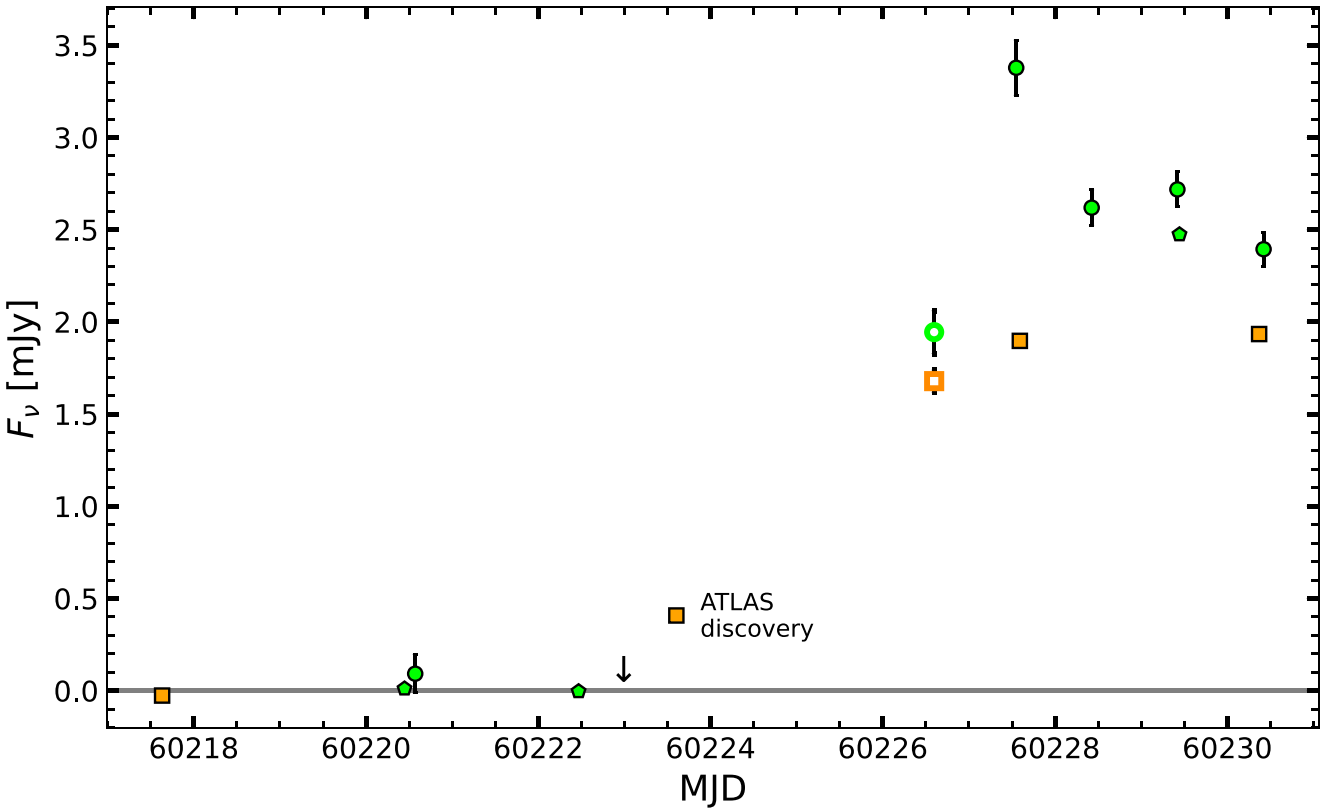

Figure 18. Early light curve of SN 2023ufx showing the adopted time of explosion (t_{exp}) marked with a downwards arrow. Only *g*-band and *o*-band light curves are shown for clarity. Open symbols are synthesized from the first SNIFS spectrum.

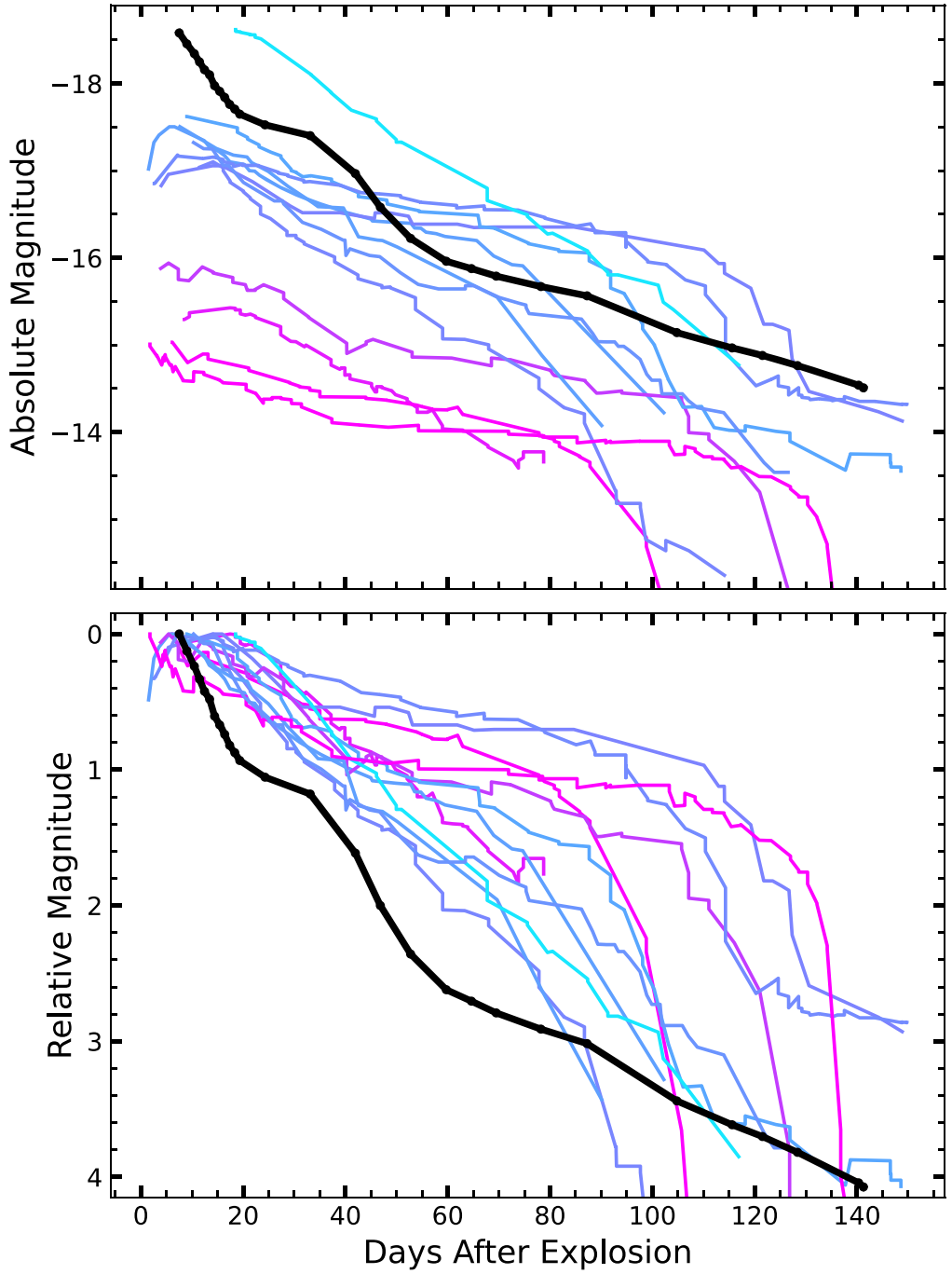

Figure 19. Comparing the *g*-band light curve of SN 2023ufx (black) to the sample from S. Valenti et al. (2016). We show the absolute magnitudes (top) and the magnitudes relative to peak (bottom) color coded according to peak absolute magnitude.

Table 5
References for Comparison Type II Supernovae

Name	References
SN 1999em	E. Baronet al. (2000), M. Hamuy et al. (2001), D. C. Leonard et al. (2002), D. Pooley et al. (2002) A. Elmhamdi et al. (2003), T. Faran et al. (2014)
SN 2006ai	D. Hiramatsu et al. (2021)
SN 2006Y	D. Hiramatsu et al. (2021)
SN 2012aw	U. Munari et al. (2013), S. Bose et al. (2013), M. Dall'Ora et al. (2014), A. A. Nikiforova et al. (2021), S. Schulze et al. (2021)
SN 2012ec	J. R. Maund et al. (2013), C. Barbarino et al. (2015), S. J. Smartt et al. (2015), M. J. Childress et al. (2016)
SN 2013ej	S. Valenti et al. (2014), M. W. Richmond (2014), S. Bose et al. (2015), F. Huang et al. (2015), G. Dhungana et al. (2016) F. Yuan et al. (2016)
SN 2014G	S. Bose et al. (2016), G. Terreran et al. (2016)
SN 2016egz	D. Hiramatsu et al. (2021)
SN 2017gmr	J. E. Andrews et al. (2019)
SN 2017ivv	C. P. Gutiérrez et al. (2020)

ORCID iDs

Michael A. Tucker https://orcid.org/0000-0002-2471-8442
Jason Hinkle https://orcid.org/0000-0001-9668-2920
Charlotte R. Angus https://orcid.org/0000-0002-4269-7999
Katie Auchettl https://orcid.org/0000-0002-4449-9152
Willem B. Hoogendam https://orcid.org/0000-0003-3953-9532
Benjamin Shappee https://orcid.org/0000-0003-4631-1149
Christopher S. Kochanek https://orcid.org/0000-0001-6017-2961
Chris Ashall https://orcid.org/0000-0002-5221-7557
Dhvanil D. Desai https://orcid.org/0000-0002-2164-859X
Aaron Do https://orcid.org/0000-0003-3429-7845
Michael D. Fulton https://orcid.org/0000-0003-1916-0664
Hua Gao https://orcid.org/0000-0003-1015-5367
Mark Huber https://orcid.org/0000-0003-1059-9603
Chien-Cheng Lin https://orcid.org/0000-0002-7272-5129
Eugene A. Magnier https://orcid.org/0000-0002-7965-2815
Bailey Martin https://orcid.org/0009-0006-4963-3206
Matt Nicholl https://orcid.org/0000-0002-2555-3192
Miika Pursiainen https://orcid.org/0000-0003-4663-4300
S. J. Smartt https://orcid.org/0000-0002-8229-1731
Ken W. Smith https://orcid.org/0000-0001-9535-3199
Shubham Srivastav https://orcid.org/0000-0003-4524-6883
Brad E. Tucker https://orcid.org/0000-0002-4283-5159
Richard J. Wainscoat https://orcid.org/0000-0002-1341-0952

References

Anderson, J. P. 2019, A&A, 628, A7
Anderson, J. P., Dessart, L., Gutierrez, C. P., et al. 2018, NatAs, 2, 574
Anderson, J. P., González-Gaitán, S., Hamuy, M., et al. 2014, ApJ, 786, 67
Anderson, J. P., Gutiérrez, C. P., Dessart, L., et al. 2016, A&A, 589, A110
Andrews, J. E., Sand, D. J., Valenti, S., et al. 2019, ApJ, 885, 43
Arcavi, I., Gal-Yam, A., Kasliwal, M. M., et al. 2010, ApJ, 721, 777
Aryan, A., Pandey, S. B., Gupta, R., & Ror, A. K. 2023, MNRAS, 521, L17
Asplund, M., Amarsi, A. M., & Grevesse, N. 2021, A&A, 653, A141
Astropy Collaboration, Price-Whelan, A. M., Lim, P. L., et al. 2022, ApJ, 935, 167
Astropy Collaboration, Price-Whelan, A. M., Sipőcz, B. M., et al. 2018, AJ, 156, 123
Astropy Collaboration, Robitaille, T. P., Tollerud, E. J., et al. 2013, A&A, 558, A33
Barbarino, C., Dall'Ora, M., Botticella, M. T., et al. 2015, MNRAS, 448, 2312
Barbary, K. 2016, extinction v0.3.0, Zenodo, doi:10.5281/zenodo.804967
Barker, B. L., Harris, C. E., Warren, M. L., O'Connor, E. P., & Couch, S. M. 2022, ApJ, 934, 67
Baron, E., Branch, D., Hauschildt, P. H., et al. 2000, ApJ, 545, 444
Bellm, E. C., Kulkarni, S. R., Graham, M. J., et al. 2019, PASP, 131, 018002
Berg, D. A., Skillman, E. D., Marble, A. R., et al. 2012, ApJ, 754, 98
Boian, I., & Groh, J. H. 2019, A&A, 621, A109
Bose, S., Kumar, B., Misra, K., et al. 2016, MNRAS, 455, 2712
Bose, S., Kumar, B., Sutaria, F., et al. 2013, MNRAS, 433, 1871
Bose, S., Sutaria, F., Kumar, B., et al. 2015, ApJ, 806, 160
Bostroem, K. A., Valenti, S., Horesh, A., et al. 2019, MNRAS, 485, 5120
Boyett, K., Mascia, S., Pentericci, L., et al. 2022, ApJL, 940, L52
Breeveld, A. A., Curran, P. A., Hoversten, E. A., et al. 2010, MNRAS, 406, 1687
Bruch, R. J., Gal-Yam, A., Yaron, O., et al. 2023, ApJ, 952, 119
Cano, Z., Wang, S.-Q., Dai, Z.-G., & Wu, X.-F. 2017, AdAst, 2017, 8929054
Carnall, A. C. 2017, arXiv:1705.05165
Carr, A., Davis, T. M., Camilleri, R., et al. 2024, PASA, 41, e608
Caswell, T. A., Droettboom, M., Lee, A., et al. 2022, matplotlib/matplotlib: REL: v3.5.2, Zenodo, doi: 10.5281/zenodo.6513224
Chambers, K. C., Magnier, E. A., Metcalfe, N., et al. 2016, arXiv:1612.05560
Chevalier, R. A., & Soderberg, A. M. 2010, ApJL, 711, L40
Childress, M. J., Tucker, B. E., Yuan, F., et al. 2016, PASA, 33, e055
Childress, M. J., Vogt, F. P. A., Nielsen, J., & Sharp, R. G. 2014, Ap&SS, 349, 617
Chornock, R., Filippenko, A. V., Li, W., & Silverman, J. M. 2010, ApJ, 713, 1363
Chrimes, A., Jonker, P., Levan, A., & Malesani, D. B. 2023, TNSAN, 292, 1
Chun, S.-H., Yoon, S.-C., Jung, M.-K., Kim, D. U., & Kim, J. 2018, ApJ, 853, 79
Couch, S. M., & Ott, C. D. 2015, ApJ, 799, 5
Couch, S. M., Wheeler, J. C., & Milosavljević, M. 2009, ApJ, 696, 953
Curti, M., D'Eugenio, F., Carniani, S., et al. 2023, MNRAS, 518, 425
Cushing, M. C., Vacca, W. D., & Rayner, J. T. 2004, PASP, 116, 362
Dall'Ora, M., Botticella, M. T., Pumo, M. L., et al. 2014, ApJ, 787, 139
Davis, S., Hsiao, E. Y., Ashall, C., et al. 2019, ApJ, 887, 4
de Jager, C., Nieuwenhuijzen, H., & van der Hucht, K. A. 1988, A&AS, 72, 259
Dessart, L., Gutierrez, C. P., Ercolino, A., Jin, H., & Langer, N. 2024, A&A, 685, A169
Dessart, L., Gutierrez, C. P., Hamuy, M., et al. 2014, MNRAS, 440, 1856
Dessart, L., & Hillier, D. J. 2022, A&A, 660, L9
Dessart, L., Hillier, D. J., & Audit, E. 2017, A&A, 605, A83
Dessart, L., Hillier, D. J., Waldman, R., & Livne, E. 2013, MNRAS, 433, 1745
Dhungana, G., Kehoe, R., Vinko, J., et al. 2016, ApJ, 822, 6
Dopita, M., Hart, J., McGregor, P., et al. 2007, Ap&SS, 310, 255
Dopita, M., Rhee, J., Farage, C., et al. 2010, Ap&SS, 327, 245
Eisenstein, D. J., Weinberg, D. H., Agol, E., et al. 2011, AJ, 142, 72
Eldridge, J. J., Xiao, L., Stanway, E. R., Rodrigues, N., & Guo, N. Y. 2018, PASA, 35, e049
Elmhamdi, A., Danziger, I. J., Chugai, N., et al. 2003, MNRAS, 338, 939
Ergon, M., Sollerman, J., Fraser, M., et al. 2014, A&A, 562, A17
Falk, S. W., & Arnett, W. D. 1977, ApJS, 33, 515
Fang, Q., Maeda, K., Ye, H., Moriya, T., & Matsumoto, T. 2024, arXiv:2404.01776
Faran, T., Poznanski, D., Filippenko, A. V., et al. 2014, MNRAS, 442, 844
Fitzpatrick, E. L. 1999, PASP, 111, 63
Fraser, M. 2016, MNRAS, 456, L16
Fruchter, A. S., Levan, A. J., Strolger, L., et al. 2006, Natur, 441, 463

Galbany, L., Anderson, J. P., Rosales-Ortega, F. F., et al. 2016, MNRAS, 455, 4087
Ganss, R., Pledger, J. L., Sansom, A. E., et al. 2022, MNRAS, 512, 1541
Gehrels, N., Chincarini, G., Giommi, P., et al. 2004, ApJ, 611, 1005
Gilkis, A., & Arcavi, I. 2022, MNRAS, 511, 691
Goldberg, J. A., Bildsten, L., & Paxton, B. 2019, ApJ, 879, 3
Gonzalez-Gaitan, S., Tominaga, N., Molina, J., et al. 2015, MNRAS, 451, 2212
Götberg, Y., de Mink, S. E., & Groh, J. H. 2017, A&A, 608, A11
Graham, J. F. 2019, arXiv:1905.13197
Guillochon, J., Parrent, J., Kelley, L. Z., & Margutti, R. 2017, ApJ, 835, 64
Gutiérrez, C. P., Anderson, J. P., Hamuy, M., et al. 2014, ApJL, 786, L15
Gutiérrez, C. P., Anderson, J. P., Hamuy, M., et al. 2017a, ApJ, 850, 89
Gutiérrez, C. P., Anderson, J. P., Hamuy, M., et al. 2017b, ApJ, 850, 90
Gutiérrez, C. P., Anderson, J. P., Sullivan, M., et al. 2018, MNRAS, 479, 3232
Gutiérrez, C. P., Pastorello, A., Jerkstrand, A., et al. 2020, MNRAS, 499, 974
Hamuy, M. 2003, ApJ, 582, 905
Hamuy, M., Pinto, P. A., Maza, J., et al. 2001, ApJ, 558, 615
Hartigan, P., Edwards, S., & Pierson, R. 2004, ApJ, 609, 261
Heger, A., & Woosley, S. E. 2010, ApJ, 724, 341
Heintz, K. E., Giménez-Arteaga, C., Fujimoto, S., et al. 2023, ApJL, 944, L30
Hiramatsu, D., Howell, D. A., Moriya, T. J., et al. 2021, ApJ, 913, 55
Hiramatsu, D., Matsumoto, T., Berger, E., et al. 2023, ApJ, 964, 181
Hook, I. M., Jørgensen, I., Allington-Smith, J. R., et al. 2004, PASP, 116, 425
Hsyu, T., Cooke, R. J., Prochaska, J. X., & Bolte, M. 2018, ApJ, 863, 134
Huang, F., Wang, X., Zhang, J., et al. 2015, ApJ, 807, 59
Ibeling, D., & Heger, A. 2013, ApJL, 765, L43
Izzo, L., de Ugarte Postigo, A., Maeda, K., et al. 2019, Natur, 565, 324
Jacobson-Galán, W. V., Dessart, L., Davis, K. W., et al. 2024, ApJ, 970, 189
Jacobson-Galán, W. V., Dessart, L., Jones, D. O., et al. 2022, ApJ, 924, 15
Jacobson-Galán, W. V., Dessart, L., Margutti, R., et al. 2023, ApJL, 954, L42
Jecmen, M. C., & Oey, M. S. 2023, ApJ, 958, 149
Jerkstrand, A. 2017, in Handbook of Supernovae, ed. A. W. Alsabti & P. Murdin (Cham: Springer), 795
Jerkstrand, A., Ergon, M., Smartt, S. J., et al. 2015, A&A, 573, A12
Jerkstrand, A., Fransson, C., Maguire, K., et al. 2012, A&A, 546, A28
Jerkstrand, A., Smartt, S. J., Fraser, M., et al. 2014, MNRAS, 439, 3694
Kasen, D., & Woosley, S. E. 2009, ApJ, 703, 2205
Kee, N. D., Sundqvist, J. O., Decin, L., de Koter, A., & Sana, H. 2021, A&A, 646, A180
Kelly, P. L., & Kirshner, R. P. 2012, ApJ, 759, 107
Kerzendorf, W. E., Do, T., de Mink, S. E., et al. 2019, A&A, 623, A34
Keszthelyi, Z., de Koter, A., Götberg, Y., et al. 2022, MNRAS, 517, 2028
Khazov, D., Yaron, O., Gal-Yam, A., et al. 2016, ApJ, 818, 3
Kifonidis, K., Plewa, T., Janka, H. T., & Müller, E. 2003, A&A, 408, 621
Kilpatrick, C. D., & Foley, R. J. 2018, MNRAS, 481, 2536
Kobulnicky, H. A., & Fryer, C. L. 2007, ApJ, 670, 747
Kochanek, C. S. 2018, MNRAS, 473, 1633
Kochanek, C. S. 2019, MNRAS, 483, 3762
Kochanek, C. S. 2021, MNRAS, 507, 5832
Kochanek, C. S. 2023, MNRAS, 519, 3865
Kochanek, C. S., Fraser, M., Adams, S. M., et al. 2017, MNRAS, 467, 3347
Kriek, M., van Dokkum, P. G., Labbé, I., et al. 2009, ApJ, 700, 221
Kron, R. G. 1980, ApJS, 43, 305
Krühler, T., Malesani, D., Fynbo, J. P. U., et al. 2015, A&A, 581, A125
Kuncarayakti, H., Anderson, J. P., Galbany, L., et al. 2018, A&A, 613, A35
Kuncarayakti, H., Doi, M., Aldering, G., et al. 2013, AJ, 146, 31
Lang, D., Hogg, D. W., Mierle, K., Blanton, M., & Roweis, S. 2010, AJ, 139, 1782
Langer, N. 2012, ARA&A, 50, 107
Lantz, B., Aldering, G., Antilogus, P., et al. 2004, Proc. SPIE, 5249, 146
Leonard, D. C., & Filippenko, A. V. 2001, PASP, 113, 920
Leonard, D. C., Filippenko, A. V., Gates, E. L., et al. 2002, PASP, 114, 35
Li, W., Van Dyk, S. D., Filippenko, A. V., & Cuillandre, J.-C. 2005, PASP, 117, 121
Limongi, M., & Chieffi, A. 2018, ApJS, 237, 13
Lopez, L. A., Ramirez-Ruiz, E., Badenes, C., et al. 2009, ApJL, 706, L106
Maeda, K., Kawabata, K., Mazzali, P. A., et al. 2008, Sci, 319, 1220
Maeder, A., & Meynet, G. 2000, ARA&A, 38, 143
Maeder, A., & Meynet, G. 2014, ApJ, 793, 123
Maguire, K., Jerkstrand, A., Smartt, S. J., et al. 2012, MNRAS, 420, 3451
Markova, N., Puls, J., & Langer, N. 2018, A&A, 613, A12
Martin, D. C., Fanson, J., Schiminovich, D., et al. 2005, ApJL, 619, L1
Martinez, L., & Bersten, M. C. 2019, A&A, 629, A124
Martinez, L., Anderson, J. P., Bersten, M. C., et al. 2022a, A&A, 660, A42
Martinez, L., Bersten, M. C., Anderson, J. P., et al. 2022b, A&A, 660, A40
Martinez, L., Bersten, M. C., Anderson, J. P., et al. 2022c, A&A, 660, A41
Mattila, S., Smartt, S. J., Eldridge, J. J., et al. 2008, ApJL, 688, L91
Maund, J. R., Arcavi, I., Ergon, M., et al. 2015, MNRAS, 454, 2580
Maund, J. R., Fraser, M., Smartt, S. J., et al. 2013, MNRAS, 431, L102
Maund, J. R., Reilly, E., & Mattila, S. 2014, MNRAS, 438, 938
Maund, J. R., Smartt, S. J., Kudritzki, R. P., Podsiadlowski, P., & Gilmore, G. F. 2004, Natur, 427, 129
Mazzali, P. A., Kawabata, K. S., Maeda, K., et al. 2005, Sci, 308, 1284
McCully, C., & Tewes, M., 2019 Astro-SCRAPPY: Speedy Cosmic Ray Annihilation Package in Python, Astrophysics Source Code Library, ascl:1907.032
Meza, N., & Anderson, J. P. 2020, A&A, 641, A177
Milisavljevic, D., Fesen, R. A., Chevalier, R. A., et al. 2012, ApJ, 751, 25
Modjaz, M., Bianco, F. B., Siwek, M., et al. 2020, ApJ, 892, 153
Modjaz, M., Kewley, L., Bloom, J. S., et al. 2011, ApJL, 731, L4
Mokiem, M. R., de Koter, A., Vink, J. S., et al. 2007, A&A, 473, 603
Morag, J., Irani, I., Sapir, N., & Waxman, E. 2024, MNRAS, 528, 7137
Morishita, T., Stiavelli, M., Grillo, C., et al. 2024, ApJ, 971, 43
Moriya, T. J., Pruzhinskaya, M. V., Ergon, M., & Blinnikov, S. I. 2016, MNRAS, 455, 423
Morozova, V., Piro, A. L., Renzo, M., & Ott, C. D. 2016, ApJ, 829, 109
Morrissey, P., Conrow, T., Barlow, T. A., et al. 2007, ApJS, 173, 682
Morrissey, P., Matuszewski, M., Martin, D. C., et al. 2018, ApJ, 864, 93
Mösta, P., Ott, C. D., Radice, D., et al. 2015, Natur, 528, 376
Müller, T., Prieto, J. L., Pejcha, O., & Clocchiatti, A. 2017, ApJ, 841, 127
Munari, U., Henden, A., Belligoli, R., et al. 2013, NewA, 20, 30
Nakajima, K., Ouchi, M., Isobe, Y., et al. 2023, ApJS, 269, 33
Neugent, K. F. 2021, ApJ, 908, 87
Neugent, K. F., Levesque, E. M., Massey, P., Morrell, N. I., & Drout, M. R. 2020, ApJ, 900, 118
Newville, M., Otten, R., Nelson, A., et al. 2021, lmfit/lmfit-py: v1.0.3, Zenodo, doi:10.5281/zenodo.5570790
Nikiforova, A. A., Baklanov, P. V., Blinnikov, S. I., et al. 2021, MNRAS, 504, 3544
Ou, P.-S., Chen, K.-J., Chu, Y.-H., & Tsai, S.-H. 2023, ApJ, 944, 34
Papish, O., & Soker, N. 2011, MNRAS, 416, 1697
Pejcha, O., & Prieto, J. L. 2015, ApJ, 806, 225
Pessi, P. J., Anderson, J. P., Folatelli, G., et al. 2023, MNRAS, 523, 5315
Pessi, T., Anderson, J. P., Lyman, J. D., et al. 2023, ApJL, 955, L29
Pogge, R. W., Atwood, B., Brewer, D. F., et al. 2010, Proc. SPIE, 7735, 77350A
Poole, T. S., Breeveld, A. A., Page, M. J., et al. 2008, MNRAS, 383, 627
Pooley, D., Lewin, W. H. G., Fox, D. W., et al. 2002, ApJ, 572, 932
Popov, D. V. 1993, ApJ, 414, 712
Prieto, J. L., Stanek, K. Z., & Beacom, J. F. 2008, ApJ, 673, 999
Prochaska, J., Hennawi, J., Westfall, K., et al. 2020, JOSS, 5, 2308
Pursiainen, M., Srivastav, S., Smartt, S. J., et al. 2023, TNSAN, 278, 1
Rabinak, I., & Waxman, E. 2011, ApJ, 728, 63
Rayner, J. T., Toomey, D. W., Onaka, P. M., et al. 2003, PASP, 115, 362
Richmond, M. W. 2014, JAVSO, 42, 333
Rizzo Smith, M., Kochanek, C. S., & Neustadt, J. M. M. 2023, MNRAS, 523, 1474
Rodríguez, Ó. 2022, MNRAS, 515, 897
Roming, P. W. A., Kennedy, T. E., Mason, K. O., et al. 2005, SSRv, 120, 95
Ryder, S. D., Van Dyk, S. D., Fox, O. D., et al. 2018, ApJ, 856, 83
Sana, H., de Mink, S. E., de Koter, A., et al. 2012, Sci, 337, 444
Sander, A. A. C., Vink, J. S., & Hamann, W. R. 2020, MNRAS, 491, 4406
Sanders, N. E., Levesque, E. M., & Soderberg, A. M. 2013, ApJ, 775, 125
Sanders, N. E., Soderberg, A. M., Gezari, S., et al. 2015, ApJ, 799, 208
Sanyal, D., Langer, N., Szécsi, D., -C Yoon, S., & Grassitelli, L. 2017, A&A, 597, A71
Sapir, N., & Waxman, E. 2017, ApJ, 838, 130
Schlafly, E. F., & Finkbeiner, D. P. 2011, ApJ, 737, 103
Schulze, S., Yaron, O., Sollerman, J., et al. 2021, ApJS, 255, 29
Scott, S., Nicholl, M., Blanchard, P., Gomez, S., & Berger, E. 2019, ApJL, 870, L16
Shappee, B. J., Prieto, J. L., Grupe, D., et al. 2014, ApJ, 788, 48
Shaya, E. J., Tully, R. B., Pomarède, D., & Peel, A. 2022, ApJ, 927, 168
Shenar, T., Sana, H., Mahy, L., et al. 2022, A&A, 665, A148
Shivvers, I., Mazzali, P., Silverman, J. M., et al. 2013, MNRAS, 436, 3614
Singh, A., Srivastav, S., Kumar, B., Anupama, G. C., & Sahu, D. K. 2018, MNRAS, 480, 2475
Smartt, S. J. 2009, ARA&A, 47, 63
Smartt, S. J., Eldridge, J. J., Crockett, R. M., & Maund, J. R. 2009, MNRAS, 395, 1409
Smartt, S. J., Maund, J. R., Hendry, M. A., et al. 2004, Sci, 303, 499

Smartt, S. J., Valenti, S., Fraser, M., et al. 2015, A&A, 579, A40
Smith, K. W., Smartt, S. J., Young, D. R., et al. 2020, PASP, 132, 085002
Smith, N. 2014, ARA&A, 52, 487
Srivastav, S., Smartt, S. J., Smith, K. W., et al. 2023, TNSAN, 268, 1
Stanway, E. R., Eldridge, J. J., & Chrimes, A. A. 2020, MNRAS, 497, 2201
Sukhbold, T., Ertl, T., Woosley, S. E., Brown, J. M., & Janka, H. T. 2016, ApJ, 821, 38
Sukhbold, T., & Woosley, S. E. 2014, ApJ, 783, 10
Svensson, K. M., Levan, A. J., Tanvir, N. R., Fruchter, A. S., & Strolger, L. G. 2010, MNRAS, 405, 57
Sweeney, D., Tuthill, P., Sharma, S., & Hirai, R. 2022, MNRAS, 516, 4971
Taddia, F., Moquist, P., Sollerman, J., et al. 2016, A&A, 587, L7
Taggart, K., & Perley, D. A. 2021, MNRAS, 503, 3931
Terreran, G., Jerkstrand, A., Benetti, S., et al. 2016, MNRAS, 462, 137
The pandas development team 2024, pandas-dev/pandas: Pandas, v2.2.2, Zenodo, doi:10.5281/zenodo.3509134
Tinyanont, S., Foley, R. J., Taggart, K., et al. 2024, PASP, 136, 014201
Tonry, J. L., Denneau, L., Flewelling, H., et al. 2018a, ApJ, 867, 105
Tonry, J. L., Denneau, L., Heinze, A. N., et al. 2018b, PASP, 130, 064505
Topping, M. W., Stark, D. P., Endsley, R., et al. 2022, ApJ, 941, 153
Tucker, M. A. 2023, TNSAN, 269, 1
Tucker, M. A., Shappee, B. J., Huber, M. E., et al. 2022, PASP, 134, 124502
Utrobin, V. P., Wongwathanarat, A., Janka, H. T., & Müller, E. 2017, ApJ, 846, 37
Valenti, S., Howell, D. A., Stritzinger, M. D., et al. 2016, MNRAS, 459, 3939
Valenti, S., Sand, D., Pastorello, A., et al. 2014, MNRAS, 438, L101
van der Walt, S., Colbert, S. C., & Varoquaux, G. 2011, CSE, 13, 22
Van Dyk, S. D., de Graw, A., Baer-Way, R., et al. 2023, MNRAS, 519, 471
Vink, J. S. 2022, ARA&A, 60, 203
Vink, J. S., de Koter, A., & Lamers, H. J. G. L. M. 2001, A&A, 369, 574
Virtanen, P., Gommers, R., Oliphant, T. E., et al. 2020, NatMe, 17, 261
Volpato, G., Marigo, P., Costa, G., et al. 2023, ApJ, 944, 40
Wongwathanarat, A., Janka, H. T., & Müller, E. 2013, A&A, 552, A126
Wongwathanarat, A., Müller, E., & Janka, H. T. 2015, A&A, 577, A48
Woosley, S. E., & Bloom, J. S. 2006, ARA&A, 44, 507
Wright, E. L., Eisenhardt, P. R. M., Mainzer, A. K., et al. 2010, AJ, 140, 1868
Yaron, O., & Gal-Yam, A. 2012, PASP, 124, 668
York, D. G., Adelman, J., John E., J., et al. 2000, AJ, 120, 1579
Yuan, F., Jerkstrand, A., Valenti, S., et al. 2016, MNRAS, 461, 2003
Yusof, N., Hirschi, R., Meynet, G., et al. 2013, MNRAS, 433, 1114
Zhang, X., Wang, X., Sai, H., et al. 2022, MNRAS, 513, 4556